Both male and female gametogenesis require a fully functional Protein *S*-Acyl Transferase 21 in *Arabidopsis thaliana*

Yaxiao Li[1,2], Hong-Ju Li[3], Chris Morgan[4], Kirsten Bomblies[5], Weicai Yang[3], Baoxiu Qi[1,6*]

[1]Department of Biology and Biochemistry, University of Bath, Claverton Down, Bath BA2 7AY, UK

[2]Current address: National Key Laboratory of Plant Molecular Genetics, Shanghai Center for Plant Stress Biology, CAS Center for Excellence in Molecular Plant Sciences Chinese Academy of Sciences (CAS), Shanghai, China

[3]Centre for Plant Gene Research, Institute of Genetics and Developmental Biology, China Academy of Science, Lincui East Road, Chaoyang District, Beijing, 100101, China

[4]Department of Cell and Developmental Biology, John Innes Centre, Norwich, NR4 7UH, UK

[5]Institute of Molecular Plant Biology, Department of Biology, ETH Zürich, Zürich, Switzerland

[6]School of Pharmacy and Biomolecular Sciences, Liverpool John Moores University, James Parsons Building, Byrom Street, Liverpool, L3 3AF, UK

*Author for correspondence

Baoxiu Qi

Email: b.qi@ljmu.ac.uk

SUMMARY

S-acylation is a reversible posttranslational lipid modification in which a long chain fatty acid covalently attaches to specific cysteine(s) of proteins via a thioester bond. It enhances the hydrophobicity of proteins, contributes to their membrane association and plays roles in protein trafficking, stability and signalling. A family of Protein S-Acyl Transferases (PATs) are responsible for this reaction. PATs are multi-pass transmembrane proteins that possess a catalytic Asp-His-His-Cys cysteine-rich domain (DHHC-CRD). In Arabidopsis there are currently 24 such PATs, five having been characterised, revealing their important roles in growth, development, senescence and stress responses. Here we report the functional characterisation of another PAT, AtPAT21, demonstrating the roles it plays in Arabidopsis sexual reproduction. Loss-of-function mutation by T-DNA insertion in *AtPAT21* results in the complete failure of seed production. Detailed studies revealed that the sterility of the mutant is caused by defects in both male and female sporogenesis and gametogenesis. To determine if the sterility observed in *atpat21-1* was caused by upstream defects in meiosis we assessed meiotic progression in pollen mother cells and found massive chromosome fragmentation and the absence of synapsis in the initial stages of meiosis. Interestingly, the fragmentation phenotype was substantially reduced in *atpat21-1 spo11-1* double mutants, indicating that AtPAT21 is required for repair, but not for the formation of SPO11-induced meiotic DNA double-strand breaks (DSBs) in Arabidopsis. Our data highlights the importance of protein S-acylation in the early meiotic stages that lead to the development of male and female sporophytic reproductive structures and associated gametophytes in Arabidopsis.

Key words: Protein S-Acyl Transferase, S-acylation, palmitoylation, gametogenesis, sterility, meiosis, *Arabidopsis thaliana*

INTRODUCTION

Cells respond to and communicate with the environment through proteins that localize on the plasma membrane, such as G protein receptors (GPRs), which can transmit signals from the extracellular to intracellular domain, or *vice versa* (Casey, 1995). Not all proteins attached to the membranes are trans-membrane proteins. Many soluble proteins can also associate with membranes after specific lipid modification, such as N-myristoylation, prenylation and *S*-acylation. *S*-acylation, also known as palmitoylation, is a posttranslational lipidation of proteins. It allows for high affinity interaction with membranes that are around 10 times stronger than myristoylation and 100 times stronger than farnesylation (Silvius and l'Heureux, 1994; Hemsley, 2009). In contrast to myristoylation and prenylation, S-acylation is reversible with palmitate (C16:0), or other long chain fatty acids, being attached to specific cysteine residue(s) of a target protein via a thioester bond (Resh, 2006; Greaves & Chamberlain, 2011). *S*-acylation is often coupled with myristoylation or prenylation, facilitating membrane attachment and trafficking of otherwise soluble proteins. Integral trans-membrane proteins can also be palmitoylated (Bijlmakers & Marsh, 2003; Blaskovic *et al.*, 2013). In this case palmitoylation can alter the structure of the transmembrane domains, regulate the association with lipid rafts and affect interactions with other proteins or other lipid modifications (Blaskovic *et al.*, 2013). Another function of palmitoylation is to protect proteins from ubiquitination and subsequent degradation (Valdez-Taubas and Pelham, 2005; Blaskovic *et al.*, 2013).

Protein *S*-acylation is catalysed by Protein *S*-Acyl Transferases (PATs). PATs are transmembrane proteins containing 4-6 transmembrane domains and an approximately 50 amino acid long, highly conserved Asp-His-His-Cys Cysteine-Rich Domain (DHHC-CRD), where the enzyme activity is believed to reside. A large scale genomic survey of 31 fully sequenced plant genomes found varying numbers of DHHC-CRD-containing sequences per plant genome and a total of 804 putative PATs were identified (Yuan *et al.*, 2013). At present, only 5 plant PATs have been studied in some detail - AtPAT24 (TIP1) (Hemsley *et al.*, 2005), AtPAT10 (Qi *et al.*, 2013; Zhou *et al.*, 2013), AtPAT13 (Lai *et al.*, 2015), AtPAT14 (Lai *et al.*, 2015; Li *et al.*, 2016; Zhao *et al.*, 2016) and AtPAT4 (Wan et al., 2017). They are all from the model plant *Arabidopsis thaliana* in which at least 24 putative PATs are found (Hemsley *et al.*, 2005; Batistič, 2012). These studies have shown that PATs play important roles in growth, development, senescence and stress responses in Arabidopsis.

Here, we report the functional characterization of a largely unknown PAT from Arabidopsis, AtPAT21. We first show that AtPAT21 has PAT activity using *in vitro* biochemical assays and *in vivo* complementation studies in yeast and in Arabidopsis. To study the biological function of AtPAT21 we isolated a T-DNA insertion transcriptional null mutant line, named *atpat21-1*, and found that it has growth defects and is sterile. To understand the sterility exhibited by the *atpat21-1* mutant, we studied both developmental and pollination related aspects of the phenotype. We found that both male and female sporophytes and gametophytes of the mutant are defective and together these lead to failure in seed production. Our results clearly demonstrate that AtPAT21-mediated protein S-acylation plays a crucial role in both male and female gametogenesis and perhaps other aspects of reproduction in Arabidopsis.

96 **RESULTS**

97 **AtPAT21 shares highly conserved sequence motifs with other known DHHC-**
98 **CRD PATs**

99 *AtPAT21* (At2g33640) encodes a 61 kDa protein making it the 5th largest (after AtPAT19,
100 AtPAT20, AtPAT24, and AtPAT22) of the 24 PATs identified in Arabidopsis. The most
101 noticeable feature of AtPAT21 is that it has an extreme C-terminal extension (Batistič, 2012).
102 AtPAT21 is predicted (by TMHMM v2.0) to possess 4 trans-membrane domains (TMD) that
103 are located between the 12-34th, 44-66th, 189-211st and 240-262nd amino acid positions,
104 respectively. The DHHC-CRD domain, which is the core catalytic S-acyl transferase functional
105 domain, is located between the second and the third TMDs and is predicted to be cytosolic. A
106 short N-terminal region and the extended C-terminal domain are also predicted to be cytosolic
107 (Figure S1a; Batistic, 2012).
108 Protein sequence alignment shows that AtPAT21 shares high homology within the DHHC-
109 CRD regions to other known DHHC-CRD PATs from Arabidopsis, yeast and mammals.
110 Outside of this region only very low homology was found (Figure S1b). Other conserved
111 regions/motifs, such as the DPG and TTxE (Mitchell *et al.*, 2006), are also found in the
112 AtPAT21 sequence (data not known, Batistic, 2012).

113

114 **PAT21 is an *S*-acyl transferase**

115 Complementation assays using the yeast PAT AKR1 knockout mutant *akr1* have been used
116 previously to test the enzyme activity of 3 plant PATs (Hemsley *et al.*, 2005; Qi *et al.*, 2013; Li
117 *et al.*, 2016). Although the restoration of temperature sensitivity of *akr1* requires both the
118 ankyrin repeats and S-acyltransferase function of the AKR1 protein (Hemsley and Grierson,
119 2011) both AtPAt10 and AtPAT14, which lack the N-terminal ankyrin repeats, can nevertheless
120 partially rescue the growth defect of *akr1*, and this was largely dependent on its S-
121 acyltransferase function (Qi et al., 2013; Li et al., 2016). To determine if AtPAT21 (again, lacks
122 the ankrin repeats) also has *S*-Acyl transferase activity we transformed pYES-AtPAT21 into
123 *akr1* yeast cells. We observed the cell phenotype of transgenic *akr1* mutants compared with
124 wild-type (WT) at the non-permissive temperature of 37ºC. As shown in Figure 1a, WT yeast

125 cells appeared round with a single nucleus. However, the majority of *akr1* cells were elongated
126 with multiple nuclei that grew poorly compared to WT. Introducing a transgene carrying
127 AtPAT21 partially rescued these growth defects of *akr1*. The transgenic cells grew much better
128 and were rounder compared to the *akr1* cells, and they contained only one nucleus, as in WT
129 (Figure 1a). Therefore, AtPAT21 partially rescues the growth defects of *akr1*. In order to
130 determine if the S-acyl transferase activity of AtPAT21 relies on its DHHC domain, we changed
131 the cysteine residue in the DHHC domain to serine and transformed the mutant GAL1-
132 AtPAT21DHHC^{174}S into the *akr1* cells. AtPAT21DHHC^{174}S transformed *akr1* cells remained
133 elongated, contained multiple nuclei and grew as poorly as *akr1* cells (Figure 1a), showing that
134 a functional DHHC domain is necessary for AtPAT21 function, at least in yeast. This verifies
135 the result from a different yeast complementation assay that showed AtPAT21 can act as a PAT
136 to target Vac8 to tonoplast in yeast (Batistic, 2012).
137 Next, we carried out a biochemical assay to determine if AtPAT21 is auto-acylated, a
138 characteristic of all DHHC-CRD PATs characterised to date. To do this we utilised a pull-down
139 acylation assay to capture S-acylated proteins from total cell lysates derived from transgenic
140 *akr1* cells expressing either AtPAT21 or its point mutation variant AtPAT21DHHC^{174}S. We
141 detected the presence of AtPAT21 and AtPAT21DHHC^{174}S by Western blotting by virtue of V5
142 epitope tags. As shown in Figure 1b while AtPAT21 could be captured by the beads and
143 subsequently detected, demonstrating auto-acylation, AtPAT21DHHC^{174}S could not, hence it
144 is not able to attach a fatty acid, i.e., is not auto-acylated.
145 These combined results demonstrate that AtPAT21 has PAT activity and its PAT activity is
146 dependent on the cysteine residue located in the DHHC domain.
147
148

149 *AtPAT21* is expressed ubiquitously

150 Understanding the spatial and temporal expression patterns of a gene can provide important
151 clues as to its function. Therefore, we carried out RT-PCR with *GAPc* as the internal control to
152 monitor the expression levels of *AtPAT21* in roots, stems, leaves, flowers and siliques of mature
153 WT Col-0 plants. We detected *AtPAT21* transcripts in all of these tissues, but they reached their
154 highest levels in flowers (Figure S2a). This is consistent with eFP gene expression data
155 available through The Arabidopsis Information Resource (TAIR) website. To further confirm
156 the AtPAT21 expression data, we transformed WT Arabidopsis with an AtPAT21promoter:GUS

157 reporter construct. Consistent with the RT-PCR data, the AtPAT21 promoter drove expression
158 in all tissues, but again with especially strong expression in flowers (Figure S2b). Thus we
159 reasoned that AtPAT21 function might be particularly important during reproductive
160 development.

161

162 AtPAT21 is predominantly localized to the plasma membrane (PM)

163 We next examined the subcellular localization of AtPAT21 in primary roots of 7-day-old
164 transgenic seedlings expressing an AtPAT21-YFP fusion protein under the control of the
165 CaMV35S promoter. For co-localization analysis AtPAT21-YFP-containing plant lines were
166 crossed with mCherry-tagged endomembrane Wave marker lines (Geldner *et al.*, 2009). We
167 found that AtPAT21-YFP largely co-localizes (Figure 2) with the mCherry plasma membrane
168 marker, R138 (PIP1;4, Boursiac *et al.*, 2005) which is consistent with a previous study that
169 demonstrated a plasma membrane localisation of transiently expressed AtPAT21 in tobacco
170 leaves (Batistič, 2012).

171

172 Identification and characterization of AtPAT21 loss-of-function mutant

173 In order to understand the biological roles of AtPAT21 in Arabidopsis growth and development,
174 we obtained a T-DNA insertion line, SALK_016521, from the Arabidopsis Biological Resource
175 Center (ABRC). We identified homozygous T-DNA insertion plants by PCR-based genotyping.
176 By sequencing PCR products amplified by T-DNA left border (LB) primer LBb1 and gene-
177 specific primer SALK_016521RP1 we showed that the T-DNA was inserted at nt1748 within
178 the 7th exon of the gene sequence, downstream of the DHHC domain which is located between
179 nt1385 - 1396 in the 5th exon (Figure 3a). We carried out RT-PCR using total RNA isolated
180 from leaf tissue of WT plants and those homozygous for the T-DNA insertion (Figure 3b).
181 *AtPAT21* transcripts were successfully detected in WT plants, but not from the T-DNA line
182 confirming this to be a null knockout mutant line, which we named *atpat21-1*. We backcrossed
183 this line with the wild-type (Col-0) for three generations to remove any possible second site
184 insertions. The fact that we could still recover the same mutant demonstrated that the mutant
185 phenotype is indeed caused by the disruption of PAT21 due to the T-DNA insertion.

186 Phenotypic assessment of *atpat21-1* plants revealed that they display a range of
187 abnormalities that affect both vegetative and reproductive growth and development. Under
188 long days *atpat21-1* mutant plants are semi-dwarf. Their leaves are smaller than WT and also
189 have a rough surface (Figure 3c-e). Generally, the epidermal cells of the mutant rosette leaves
190 are much smaller than those of WT (Figure S3). Strikingly, the mature siliques of *atpat21-1* are
191 very short and do not contain any seeds, and have only what appear to be shrivelled ovules
192 (Figure 4S). Thus, *atpat21-1* is completely sterile. The mutant has a prolonged growth period
193 (>2 months) which may in part result from being sterile. In addition, the mutant plants are more
194 branched than WT (Table S1).
195 In order to confirm that AtPAT21 loss-of-function caused the growth defects of *atpat21-1*,
196 we transformed heterozygous mutant plants with 35S:AtPAT21. Through PCR-based
197 genotyping, we identified 35S:AtPAT21 transgenic plants that were homozygous for the
198 *atpat21-1* mutation and these plants were indistinguishable to WT. However, when we used a
199 construct carrying a cysteine to serine mutation in the DHHC domain (AtPAT21DHHC^{174}S),
200 the *atpat21-1* phenotype was not rescued (Figure 3f). These results clearly demonstrate that the
201 aberrant phenotype of *atpat21-1* is caused by loss of AtPAT21 and that the Cys residue in the
202 DHHC domain essential for its PAT activity as we demonstrated above, is also essential for its
203 function within the plant.
204

205 **AtPAT21 loss-of-function causes male sporophytic and gametophytic defects**

206 To find out the cause of the sterility of *atpat21-1* mutant plants, we first observed the anthers
207 and pollen grains from mature flowers of WT and *atpat21-1* mutant plants (Figure 4). In WT
208 flowers the stigma is encircled by anthers and covered by pollen grains (Figure 4a-b), whereas
209 stigmas of the *atpat21-1* mutant were devoid of pollen grains and the relative positioning of
210 the anthers and stigma was different, such that anthers were shorter and held below the level
211 of the stigma. Importantly, mutant anthers failed to dehisce and release pollen grains (Figure
212 4d-e) suggesting sterility arises from earlier defects in meiosis and/or pollen development,
213 rather than purely from positional defects. Analysis of the pollen from *atpat21-1* anthers
214 revealed markedly reduced size compared to WT pollen, and with nuclei being generally absent
215 (16.1 ±1.5μM in mutant compared to 32.5±1.5μM in WT, see Figure 4c and f). The small
216 proportion of mutant pollen grains that did contain two sperm cell nuclei were also much
217 smaller than WT pollen grains.

218 To determine at what point pollen development is perturbed in *atpat21-1*, we embedded
219 floral material covering all stages of anther development in plastic, sectioned and imaged with
220 WT as control (Figure 5). We found that the mutant microsporocytes were able to complete
221 meiosis but normal 'tetrads' were not formed, rather, asymmetrical polyads containing 2-6
222 microspores made up the majority of meiotic products. Microspores were successfully released
223 from polyads (Figure 5g), however the sizes of released mutant pollen grains were not identical
224 and the majority degenerated soon thereafter (Figure 5h). Direct observation of the anthers at
225 this stage also confirmed these findings (Figure S5). These may explain the large proportion of
226 the shrivelled pollen grains that we observed in *atpat21-1* mutant anthers (Figure 4e).

227

228 **AtPAT21 loss-of-function causes female gametophytic defects**

229 To determine whether *atpat21-1* is also defective in female sporophytic and/or gametophytic
230 development we next observed and compared the pistils from fully opened flowers in the
231 mutant and WT plants. The mutant had smaller ovules than WT (40.0±3.6μM in mutant
232 compared to 76.36±5.6μM in WT, Figure 6a top panel). To check whether ovules in mutant
233 plants were functional, we carried out manual pollinations using pollen from WT plants.
234 Following pollination, we observed the development of mutant and WT ovules at 1, 2 and 15
235 days after pollination (DAP) (Figure 6a). At 1 and 2 DAP WT ovules became enlarged and a
236 globular embryo was clearly visible (arrows in Figure 6a, the second and third panels on the
237 left). However, *atpat21-1* ovules lacked an embryo although they did show an increase in
238 overall size by 2 DAP (Figure 6a, the second and third panels on the right). By 3 DAP, WT
239 ovules continued to enlarge whilst mutant ovules appeared to abort and were completely
240 shrivelled. On maturity at 15 DAP WT siliques had a full set of ~55 seeds whereas no seeds
241 were present in *atpat21-1* siliques (Figure 6a bottom panel). This suggests that *atpat21-1* has
242 defects in either supporting the growth or guidance of WT pollen tubes and/or that *atpat21-1*
243 ovules fail to produce a normal female gametophyte capable of double fertilisation and
244 subsequent seed development.
245 To determine the cause of female sterility we observed pollen tube growth in the stigmas
246 and styles of both WT and *atpat21-1* plants at 15 hours after pollination with WT pollen. The
247 WT pollen grains had germinated and pollen tubes had penetrated both the *atpat21-1* and WT
248 stigmas (arrowheads in the left pictures, Figure 6b). At this stage there was no observable

249 difference between WT pollen tubes (arrows in the left pictures, Figure 6b) transmitting
250 through the styles of *atpat21-1* or WT plants, clearly indicating that mutant stigmas were
251 capable of supporting pollen tube growth. However, although pollen tubes (arrows) could be
252 seen entering the WT ovule via the micropyle (arrowhead) no pollen tubes were observed to
253 enter *atpat21-1* ovules (Figure 6b right panel). Therefore, mutant *atpat21-1* ovules most likely
254 fail to provide the appropriate guidance cues to WT pollen tubes. These data further support
255 the proposition that mutant ovules fail to produce pollen tube guidance cues, suggesting that
256 appropriate development of ovules may be perturbed in *atpat21-1* plants. Therefore, these
257 combined results clearly demonstrated that *atpat21-1* has catastrophic female gametophytic
258 defects, resulting in its sterility.
259

260 Both male and female gametophytic defects are partially independent of 261 their sporophytic defects in *atpat21-1*

262 Gametophytic defects can be caused either by the effects of a mutation in diploid sporophytic
263 tissues such as in stamens or pistils, or independently of the sporophyte if the disruption appears
264 after meiosis (McCormick, 2004). For sporophyte independent gametophytic defects these
265 must be maintained in heterozygotes (McCormick, 2004). To determine if the observed
266 gametophytic defects were present in plants heterozygous for *atpat21-1* we genotyped
267 progenies derived from self-pollinated *atpat21-1*(+/-) plants (♀Het x ♂Het, selfed), and from
268 heterozygous *atpat21-1*(+/-) plants reciprocally crossed to WT (♀WT x ♂Het or ♀Het x ♂WT)
269 (Table 1 and Figure S6). In the progeny of self-pollinated heterozygotes, the number of WT-
270 phenotype (WT and heterozygous) plants to homozygous *atpat21-1* mutant plants was 5.2:1
271 which was higher than the expected 3:1 (Table 1). This points to a gametophytic defect existing
272 in either male or female gametes, or both. To address this we next carried out reciprocal
273 crossing between *atpat21*(+/-) plants and WT and found that when the heterozygote acted as
274 the pollen donor (♀WT x ♂Het), the ratio of WT to heterozygotes from the F1 progeny was
275 1.3:1. This is higher than the expected 1:1 ratio (Table 1) and demonstrates that not all mutant
276 pollen grains produced by *atpat21-1*(+/-) plants are viable. Around 23% of the mutant pollen
277 grains failed to fertilize WT ovules that would have subsequently developed into heterozygous
278 seeds, leading to a higher number of WT pollen grains to fertilize WT ovules hence more WT
279 seeds produced. Thus it seems that a considerable proportion of male gametophytes derived
280 from *atpat21-1*(+/-) plants were defective. On the other hand, when the reciprocal cross of ♀

281 Het x ♂WT was carried out, the number of the heterozygous plants recovered in the next
282 generation was only about half that of WT plants (AtPAT21(+/+):*atpat21-1*(+/-) = 1.9:1 instead
283 of the expected 1:1 ratio) (Table 1). This indicates that there is also a female gametophytic
284 defect(s), which is much more severe than the male defects, observable in *atpat21-1*
285 heterozygous plants. Consistent with these results, we also found some un-fertilized ovules
286 from these crosses (arrowheads, Figure S6). In contrast to what was observed in plants
287 homozygous for *atpat21-1*, both male and female gametophytes are not completely sterile in
288 the heterozygote. Thus the gametophytic effect of *atpat21-1* on sterility is not fully penetrant
289 but is enhanced by the effects of *atpat21-1(-/-)* on sporophytic tissue.

290 To further dissect the male gametophytic defects, we analysed pollen grains derived from
291 *atpat21-1*(+/-) plants. While the majority of these pollen grains exhibited a similar size and
292 appearance to WT, around 15% of them appeared much smaller (red arrows, Figure 7a, bottom
293 left). *In vitro* pollen germination assays showed that while 87.3% of WT pollen grains (n=100)
294 germinated, only 47.8% (n=100) of pollen derived from *atpat21-1*(+/-) plants produced tubes.
295 Interestingly, none of the small pollen grains germinated (red arrow, Figure 7a, bottom right).
296 These abnormal small pollen grains are unable to effect fertilisation *in vivo* and therefore
297 probably contributed to the lower numbers of homozygous or heterozygous seedlings
298 recovered when *atpat21-1*(+/-) was used as the pollen donor in the self- and reciprocal crosses
299 detailed above (Table 1). The fact that the percentage of small pollen grains was much lower
300 than 50% demonstrates that a large proportion of *atpat21-1* mutant pollen grains appear
301 phenotypically similar to WT and that these 'normal' grains are capable of effecting double
302 fertilization and subsequent seed production. Consistent with this, 43.6% of seedlings
303 recovered from "♀WT x ♂Het" crosses were *atpat21-1*(+/-), but still a 6.4% loss of fertility
304 was caused by defects in pollen carrying an *atpat21-1* allele (Table 1).

305 In summary the gametophytic defects observed in the AtPAT21 loss-of-function mutant are
306 partially related to sporophytic effects of the mutation.

307 We next phenotyped the female gametophytes in *atpat21-1*(+/-) plants. Stage 12c flowers
308 derived from WT and heterozygous plants were emasculated and fixed 24 hours later
309 permitting the female gametophyte to reach maturity (FG7, four-celled stage, Figure 7b-1). Of
310 the 221 ovules examined from *atpat21-1*(+/-) plants, 55% contained a mature female
311 gametophyte similar to that of WT, suggesting that these ovules represent predominantly WT
312 ovules. The remaining 45%, having an abnormal phenotype, likely correspond to those
313 harbouring a mutant female gametophyte. The mutant female gametophytes at this stage
314 displayed a range of abnormal phenotypes with some containing no discernible nuclei, being

reduced in size and having an accumulation of small vacuoles or presence of a larger vacuole with mis-positioned nuclei (Figure 7b-2-3). This result indicates that development of the mutant female gametophyte may be perturbed at an early stage.

To determine at which stage the lesion occurs we analysed female gametophytes in pistils from heterozygous plants (n=67) at the FG1 to FG2 developmental stage. At FG1-2, 46% of ovules exhibited normal megaspore specification and the first nuclear division (Figure 7b-4 and 5), whilst 54% of ovules displayed several defects. These included gametophytes having an irregular nucleus with higher auto-fluorescence in the cytosol (Figure 7b-6), abnormalities in the subsequent nuclear division where a central vacuole was formed but no nuclei were observed, indicating degeneration of nuclei (Figure 7b-7), and a smaller megaspore with no apparent nucleus (Figure 7b-8 and 9).

These combined results clearly demonstrate that *atpat21-1* female gametophytes have a defect that exerts its effects during megaspore specification, preventing progression into a functional 8-celled embryo sac.

AtPAT21 loss-of-function causes defects in meiotic double-strand break repair

To determine if the sterility observed in *atpat21-1* mutants was caused at least in part by upstream errors in meiosis, we assessed meiotic progression cytologically in DAPI stained chromosomal spreads from both *atpat21-1* and WT Col-0 plants. In WT meiosis, homologous chromosomes synapse during prophase I via the formation of the synaptonemal complex which is required for stable crossover formation (Figure 8a). As well as generating genetic diversity, crossovers provide points of physical connection between homologues and promote their even segregation during anaphase I (Figure 8b-d). Sister chromatids then separate during anaphase II to generate four daughter cells, each with half the original diploid chromosomal complement (Figure 8e).

Compared with WT, many meiotic errors were observed in *atpat21-1* mutants. Firstly, during prophase I homologues in the mutants completely fail to synapse and fragments of chromatin fibres were observed in some cells (Figure 8f). We also observed chromosomal fragmentation during diakinesis and metaphase I in all *atpat21-1* cells (Figure 8g,h), with chromosomes regularly clumping together in metaphase I to form a tangled-mess that contrasted with the 5 clear bivalents that are observed in WT meiosis. We also observed abnormalities in all *atpat21-1* dyad and tetrad cells (Figure 8i,j), which represent the products

of anaphase I and II, respectively. In both stages chromosome fragments were observed and missegregated chromosomes led the formation of unbalanced daughter cells and micronuclei.

The meiotic phenotype observed in *atpat21-1* was reminiscent of similar phenotypes previously observed in meiotic double-strand break (DSB) repair mutants in *A. thaliana* (e.g. (Abe et al., 2005; Bleuyard et al., 2004; Puizina et al., 2004). To determine if the meiotic errors observed in *atpat21-1* arose from failures in DSB repair, we crossed *atpat21-1* plants with *atspo11-1* plants to generate *atpat21-1/atspo11-1* double-mutants. SPO11 is required for the initial formation of DSBs early in meiosis (Grelon et al., 2001). *atspo11-1* single mutants fail to form meiotic DSBs, leading to homologue asynapsis during prophase I (Figure 8k) and a complete failure in crossover formation, producing 10 univalent chromosomes during diakinesis and metaphase I (Figure 8l,m). The univalent chromosomes readily missegregate during anaphase I leading to the formation of unbalanced dyads and tetrads later in meiosis (Figure 8n,o). In the *atpat21-1/atspo11-1* double-mutants the fragmentation phenotype observed in the *atpat21-1* single mutant was absent, showing that the presence of fragments requires DSBs produced by SPO11. Homologue asynapsis, univalent formation and chromosome missegregation were still apparent in the double mutant, as in the *atspo11-1* single mutant phenotype (Figure 8p-t). Taken together, this indicates that the chromosomal fragmentation phenotype observed in the *atpat21-1* mutant arises from a failure in the repair of SPO11 induced meiotic DSBs.

AtPAT21 loss-of-function leads to somatic genome instability

Many proteins known to function in meiotic DSB repair are also required for the repair of somatic DSBs via homologous recombination (Puizina et al., 2004). To determine if PAT21 also plays a role in the maintenance of somatic genome integrity, which could help explain the somatic phenotype of *atpat21-1* mutants, we cytologically screened mitotic anaphase cells for irregularities in both WT Col-0 and *atpat21-1* plants. In *atpat21-1* anaphase bridges or lagging chromosomes were observed in 17% (17/100) of cells (Figure 8v). Anaphase bridges and lagging chromosomes result from the formation of dicentric and acentric chromosomes, respectively, which can be generated by the misrepair of somatic DSBs. No anaphase bridges or lagging chromosomes were observed in any mitotic cells from WT Col-0 (0/100) (Figure 8u). Thus, there was a significant increase in the occurrence of lagging chromosomes in the *atpat21-1* background (p =7.3 x 10^{-6}, two-tailed Fisher's exact test). It is therefore likely that

somatic genome instability contributes to the defects observed in the vegetative growth of *atpat21-1* plants.

As AtPAT21 functions through its PAT enzyme activity (Figure 1 and S4) and SPO11 has not been shown experimentally to be palmitoylated we analysed its potential palmitoylation site(s) using the Clustering and Scoring Strategy software for the prediction of palmitoylation sites (CSS-Palm 4.0) (Zhou *et al.*, 2006; Ren *et al.*, 2008). This gave negative results, i.e., no such sites are predicted in the SPO11 sequence. Therefore, using the same software we analysed other protein sequences of over 80 genes that have been reported to have roles in the process of meiosis in plants (reviewed by Mercier *et al.*, 2015). In general, loss-of-function mutants of these genes have defects in both male and female fertility. It is possible that AtPAT21 palmitoylates one or more such proteins that are involved in the repair of SPO11-mediated DSBs during meiosis. Among these protein sequences a few scored very high and the higher the score is for a particular cysteine residue(s) within the predicted protein sequence the higher the possibility would be for this cysteine(s) to be palmitoylated. For instance, the cysteine residues at position 3 (C^3) and 6 (C^6) of HEI10 (Enhancer of cell invasion 10) were scored at 20 and 40, respectively; the ninth cysteine (C^9) of PRD1 (Putative recombination initiation defect 1) was 34 and the score of the 18th cysteine (C^{18}) of MRE11 was 26, indicating that these proteins are likely palmitoylated at these specific cysteine residues.

DISCUSSION

We report here the characterization of a protein S-acyltransferase, AtPAT21, from Arabidopsis. We showed that disruption of AtPAT21 by T-DNA insertion results in sterility and other growth and development defects in the mutant plants (Figures 3&4). We also showed that AtPAT21, which contains the characteristic DHHC-CRD domain (Figure 1S), is indeed a functional S-acyl transferase. Importantly, we showed that Cys to Ser mutation in the DHHC catalytic domain of AtPAT21 destroys its ability to restore the growth defect of yeast *akr1* lines and to auto-acylate (Figure 1). We further studied the biological function of AtPAT21 using a T-DNA knockout mutant allele, *atpat21-1* (Figure 3). The mutant plants had stunted growth and altered development, and were sterile.

The effects of mutating AtPAT21 are diverse, but are clearly particularly damaging for reproduction. First, we found some evidence that AtPAT21 might be involved in anther dehiscence, though whether this is a direct effect is not yet clear. Anthers of *atpat21-1* mutant plants fail to dehisce and as a result no pollen grains are released. We showed by scanning electron microscopy that the stomium of WT anthers was completely broken down at dehiscence, leading to the exposure and release of the anther contents, whereas the stomium in *atpat21-1* anthers remained largely intact (Figure 4). Pressure generated by swelling of a full complement of pollen grains in the anther is required to split the stomium. Indeed, anthers of the *lap5-1 lap6-1* (LESS ADHESIVE POLLEN) double mutant failed to dehisce due to the shrivelled nature of the pollen grains (Dobritsa *et al.*, 2010). This may also be the case for *atpat21-1* anthers as they contain largely degenerated pollen grains which would exert much less pressure within the anther. However, anthers of the male sterile mutant *acos5* (Acyl-CoA Synthetase 5) are still able to dehisce despite the fact that they contain shrivelled and inviable pollen grains (de Azevedo Souza *et al.*, 2009). This indicates that dehiscence of the Arabidopsis anther is more complex and does not depend on its contents alone. The fact that loss-of-function of AtPAT21 exhibits disruption in anther dehiscence demonstrates that protein *S*-acylation mediated by AtPAT21may also be involved in this important process.

We also found that male and female sterility in the *AtPAT21* loss-of-function mutant is caused by severe meiotic defects. Failure to produce pollen or the production of abnormal pollen can be caused by either meiotic defects, defects in subsequent mitoses, or abnormalities in the cell layers surrounding the locules (Sanders *et al.*, 1999). In the *atpat21-1* mutant anthers all cell layers were present and seemed to develop properly. However, the production of tetrads was abnormal with asymmetrical polyads containing 2-6 microspores being frequently observed (Figure S5). Thus, the defect caused by loss of *AtPAT21* could have affected the meiotic stage of pollen development leading to deviations from the typical number of 4 meiotic products found in tetrads of WT anthers. Ovule development in *atpat21-1* also showed severe defects that similarly seem to act at the meiotic stage of development.

Indeed, observation of DAPI stained chromosomal spreads prepared from fixed buds containing male meiocytes revealed many errors throughout meiosis in *atpat21-1* plants, leading to chromosome fragmentation, homologue missegregation and the formation of unbalanced daughter cells and micronuclei (Figure 8). Further analysis of the double mutant

atpat21-1 atspo11-1 confirmed that the meiotic defects in *atpat21-1* were due to the failure in repair of early meiotic DSBs induced by SPO11.

Our data clearly demonstrated that Arabidopsis PAT21 is involved in both male and female microsporogenesis and megasporogenesis through the repair of SPO11 induced DSBs during early stages of meiosis. Further analysis of potential palmitoylation sites in meiosis proteins suggests HEI10, PRD1, and MRE11 as especially good candidates as targets of AtPAT21. Consistent with this, the transcriptional null mutant of *HEI10* also has asymmetric tetrads or polyads containing more than four microspores (Chelysheva *et al.*, 2012); the loss-of-function mutant for *PRD1* has very short siliques that contain very few seeds (2.62 seeds/silique) and this is caused by both male and female gametogenesis or/and sporogenesis defects (De Muyt *et al.*, 2007); and the *mre11-3* mutant plants are dwarfed with shorter roots in addition to a lack of pollen grains and sterility (Bundock & Hooykaas, 2002). All of these defects have also been observed in *atpat21-1*, suggesting that some, or all, these proteins may be the palmitoylating targets of AtPAT21 in Arabidopsis. Loss-of-function of *AtPAT21* would lead to a failure in the palmitoylation of these proteins and loss of appropriate membrane localization and function resulting in the defects observed in these mutants. However, it is puzzling as to how AtPAT21 exerts its role as an S-acyltransferase since these putative substrate proteins are localized in the nucleus while AtPAT21 is localized in plasma membrane. In fact, no DHHC-PATs have been reported to localise within the nucleus. Future research will be required to determine if and how these putative palmitoylated proteins interact with AtPAT21 to shed new light on the roles played by palmitoylation in reproductive biology, especially during meiosis in Arabidopsis.

It is noteworthy that after submission of this manuscript, a new study has been published linking RIF1 S-acylation by the DHHC family palmitoyl acyltransferase Pfa4 to DSB repair in yeast (Fontana *et al*., 2019). As no RIF1 orthologue exists in plants the PAT21 mediated process must be mechanistically different. Therefore, our finding of the involvement of PAT21 in DSB repair in Arabidopsis is both relevant and timely. This may open a new area of investigation in examining how S-acylation affects nuclear/DNA events in general with a special emphasis on plants; something that has hitherto largely been ignored in any eukaryote so far.

In summary, we have shown that Protein S-Acyltransferase 21 is involved in reproduction in Arabidopsis. We identify AtPAT21 as a positive regulator of fertility and hence seed

production in Arabidopsis that acts by modulating both male and female microsporogenesis and megasporogenesis through the regulation of meiosis and mitosis.

CONCLUSIONS

In this study we demonstrated that the knock-out mutant of a single gene, AtPAT21 leads to defects ranging from vegetative growth to reproductive development. This is perhaps not surprising as AtPAT21 is ubiquitously expressed (Figure S2 and Batistič, 2012). Mutant *atpat21-1* plants have reduced stature, smaller and uneven leaves and more branching of inflorescences compared to the wild-type Col-0 Arabidopsis plants (Figure 3 and Table S1), indicating that AtPAT21 is essential for normal vegetative growth in Arabidopsis. Perhaps most strikingly, AtPAT21 loss-of-function causes both male and female sterility and the mutant plants do not produce seeds. We confirmed both in vivo and in vitro that AtPAT21 is an S-acyl transferase. Therefore, it may function through S-acylation of one or multiple target proteins that are involved in a range of processes in the plant. We focused our study on the roles of AtPAT21 in reproduction. This led to the conclusion that successful male and female microsporogenesis and megasporogenesis relies on S-acylation of proteins that participate in the regulation of meiosis and mitosis in both male and female reproductive tissues in Arabidopsis.

EXPERIMENTAL PROCEDURES

Plant material and growth conditions

Wild-type and the T-DNA insertion line SALK_016521 of *Arabidopsis thaliana* in the background of Columbia-0 (Col-0) were obtained from the Arabidopsis Biological Resources Center (ABRC, http://www.arabidopsis.org/abrc/). Seeds were surface sterilized, germinated and plants were grown under long days (LD) as described previously (Qi *et al.*, 2013).

RT- PCR and GUS staining

To detect the transcript levels of *AtPAT21* in seedlings and different parts of Arabidopsis plants total RNA was extracted from WT seedlings and leaves, stems, flowers and siliques of mature plants. First strand cDNA was synthesized and PCR was carried out using the *AtPAT21* gene specific pair of primers (Table S2).

To make the promotor-GUS expression construct about 800bp upstream of the start code of *AtPAT21* was used and amplified with a pair of primers pPAT21attB1/ pPAT21attB2 (Table S2). This DNA fragment was re-combined into the pMDC162 vector (Curtis & Grossniklaus 2003) via Gateway cloning technology to make the promotor-GUS fusion. Tissues from *proAtPAT21*:GUS transgenic plants were stained in the staining buffer (100mM Sodium phosphate buffer, pH7.0; 10mM EDTA; 0.1% triton X-100; 1Mm $K_3Fe(CN)_6$; 2mM X-Gluc) at 37°C for overnight. The samples were cleared with 100% alcohol for 12 hours and repeated several times before being observed and photographed (Jefferson, 1987).

Identification of the *AtPAT21* T-DNA insertion mutant

Homozygous T-DNA insertion mutant Arabidopsis plants were isolated and characterized according to Qi *et al* (2013) and Li *et al* (2016) using primers listed in table S2.

Complementation in yeast and Arabidopsis

To determine the PAT activity of AtPAT21, complementation assays in yeast and Arabidopsis were carried out. Briefly, the coding region of *AtPAT21* was PCR-amplified from first strand cDNA without the stop codon and cloned in the Gateway pDONR/Zeo vector (Invitrogen). To change the cysteine residue to serine in the DHHC motif a first round PCR was carried out using 2 pairs of primers, DHHCtoS For + End and Beg + DHHCtoS Rev (Table S3), followed by a second round of PCR using primer pair Beg and End to assemble the full length *DHHS-AtPAT21*. This product was again cloned into pDONR/Zeo. The *WT-PAT21* and *DHHS-PAT21* were recombined into pYES-DEST52 (C-terminal V5 fusion) (Invitrogen) and pEarleyGate 101 (C-terminal YFP fusion) (Earley *et al.*, 2006) for expression in yeast and Arabidopsis, respectively.

Transformation of *akr1* yeast cells and Arabidopsis plants and subsequent growth conditions were carried out as described previously (Qi *et al.*, 2013; Li *et al.*, 2016).

Auto-acylation assays in yeast

Twenty mL of transgenic yeast cells were grown at 25 ^{o}C in selective minimal media containing 2% galactose to induce protein expression. After 2 days the cells were collected by centrifugation. Cells were resuspended in 0.5 mL of lysis buffer (100 mM HEPES, 1.0 mM EDTA, 1x Roche complete protease inhibitor, pH 7.5) and broken open by adding 0.5 g of acid-washed sand (400-600 µM, Sigma) and votexing for 1 minute. This was repeated 4 more times with cooling on ice between each votexing step. This was followed by blocking the free –SH groups and capturing the S-acylated proteins utilizing the Acyl-RAC method (Forrester *et al.* 2011). The proteins were separated via 10% SDS-PAGE and PAT21/DHHS-PAT21 were detected by Western blot with an anti-V5 antibody (mouse monoclonal antibody, KWBio, China) and ECL as described previously (Li *et al.*, 2016).

Subcellular localization of AtPAT21

For determining subcellular localization *atpat21-1* mutant plants complemented by the 35S:AtPAT21-YFP construct were crossed with mCherry-tagged marker Wavelines (Geldner *et al.*, 2009). Primary roots of 7-day-old seedlings from the crossed F1 progeny were observed and imaged according to Qi *et al.* (2013).

Visualization and imaging of pollen tubes

Pistils, after being pollinated for 5 and 15 hours, were excised and submerged in fixing solution (10% v/v acetic acid, 30% v/v chloroform, 60% v/v ethanol) for 16 hours. The fixative was then removed and the pistils were rinsed twice for 5 minutes in 50mM potassium phosphate buffer (pH7.0) twice. The pistils were softened in 4M NaOH at room temperature for 15 minutes. They were rinsed twice in 50mM potassium phosphate buffer before being stained in aniline blue (0.1% w/v Aniline Blue in 0.1M K_3PO4, pH 11) for 1 hour followed by washing in 50mM potassium phosphate as before (modified from Kho & Baer, 1968). After removing the potassium phosphate buffer a drop of mounting media (50% glycerol in 50 mM potassium phosphate pH7.0) was applied and the pistils were transferred onto a glass slide and covered

with a coverslip. The pistils were gently squashed to expose the pollen tubes and visualized under UV light using a Nikon Eclipse 90i Eclipse epifluorescence microscope equipped with a Nikon Digital Sight DS-U1 camera for image capture.

In vitro pollen germination

Mature pollen grains from WT and heterozygous AtPAT21/*atpat21-1* flowers were collected and placed on freshly made pollen tube growth media as described above and incubated at 24℃ overnight. The germination of pollen grains was checked under a dissecting microscope. The number of germinated pollen grains were counted and calculated as percentage of total pollen grains placed on the media.

Microscopy of anthers, ovules and pollen grains

For scanning electron microscopy (SEM) of pollen grains freshly opened flowers were frozen in liquid nitrogen and freeze-dried overnight. Several anthers were taken and coated with gold. Observation and image capture was carried out using a scanning electron microscope (JSM-6480-LV).

For observation of mature ovules both unfertilized and fertilized ovules were submerged in clearing solution (Chloral hydrate (g): Glycerol (mL):ddH_2O (mL) = 8:1:3) for several hours (vary depending on the age of samples observed) prior to imaging using a Nikon Eclipse 90i microscope, as described above. For visualization of pollen grains freshly collected samples were suspended in 10% glycerol and observed directly or stained for 10 minutes in DAPI solution (0.1 M sodium phosphate, pH 7.0, 1 mM EDTA, 0.1% Triton X-100, and 0.5 µg/mL DAPI) and observed under UV light using the Nikon Eclipse 90i microscope.

For observation of pollen and ovule development inflorescences were fixed in 4% glutaraldehyde in 12.5 mM cacodylate buffer, pH 6.9, and dehydrated through a conventional ethanol series and subsequently cleared in 2:1 benzyl benzoate:benzyl alcohol. The dissection of ovules at different developmental stages was according to Chen *et al.* (2007). For sectioning floral buds were embedded in Historesin and semi-thin (0.5 µm) sections were obtained using an ultra-microtome (Leica Microsystems, Nussloch, Germany). Sections were stained with 0.05% of Toluidine Blue O for 40 to 60 seconds, and photographed under the microscope as described previously (Chen *et al.*, 2007).

Generation of *atpat21-1 spo11-1-1* double mutants

Double mutant plants of *atpat21-1 spo11-1-1* were obtained from crosses between SPO11-1-1+/- (Grelon et al., 2001) and AtPAT21+/- plants. Double mutants were identified by PCR of the F2 population obtained by selfing F1 plants heterozygous for both genes.

Cytological analysis of mitotic and meiotic chromosomes

Both meiotic and mitotic DAPI stained chromosome spreads were prepared as described previously (Caryl et al., 2000). In brief, inflorescences were fixed in 3:1 ethanol:acetic acid for at least 24 hours and fixed buds containing male meiocytes were then dissected from the main inflorescence, washed in 0.01M citrate buffer and incubated in digestion medium (0.33% pectolyase (Sigma P5936), 0.33% cellulase (Sigma C1794) dissolved in 0.01M citrate buffer) for 90 minutes at 37 °C. Digested buds were macerated with a brass rod in a drop of 65% acetic acid on a glass slide before adding another 14 µL 65% acetic acid and placing the slide on a hot plate at 45 °C for 1 minute whilst stirring with a mounted needle. Cells were then fixed to the slide by the addition of 400 µL 3:1 fixative before drying the slide and then mounting a coverslip with 7 µL 10 µg/mL DAPI in Vectashield (Vector Labs). Slides were imaged using a Zeiss Axio Imager Z2 epifluorescence microscope.

ACKNOWLEDGEMENTS

We thank the ABRC and NASC for providing Arabidopsis T-DNA insertion lines for AtPAT21 and SPO11. Thanks also go to Mrs Ursula Potter, University of Bath, UK for assisting with sample preparation and SEM observation of anthers and pollens.

This work was supported by the National Natural Science Foundation of China (Grant No. 31170233 to BQ). CM and KB were supported by a UK Biological and Biotechnology Research Council (BBSRC) grant to the John Innes Centre (BB/P013511/1), and a European Research Council Consolidator Grant to KB (EVO-MEIO 681946).

CONFLICT OF INTEREST

The authors declare that they have no conflict of interest.

SUPPORTING INFORMATION

Additional Supporting Information may be found in the online version of this article.

Table S1. Phenotypic analysis of WT and *atpat21* Arabidopsis plants
Table S2. Sequence of primers used for PCR

Figure S1. Secondary structure prediction of AtPAT21 and protein sequence alignment with some known DHHC-PATs.
Figure S2. AtPAT21 expression pattern in Arabidopsis.
Figure S3. *atpat21-1* has smaller cells.
Figure 4S. *atpat21-1* is completely sterile.
Figure S5. The *atpat21-1* mutant have asymmetrical polyads structure which will release variable sizes of pollen grains.
Figure S6. Seed set of different crosses.

REFERENCES

Abe, K., K. Osakabe, S. Nakayama, M. Endo, A. Tagiri, S. Todoriki, H. Ichikawa, and S. Toki (2005) Arabidopsis RAD51C gene is important for homologous recombination in meiosis and mitosis. *Plant Physiology*, **139**, 896-908.

Batistič, O. (2012) Genomics and Localization of the Arabidopsis DHHC-Cysteine-Rich Domain S-Acyltransferase Protein Family. *Plant Physiology*, **160**, 1597-1612.

Bijlmakers, M.J. and Marsh, M. (2003) The on–off story of protein palmitoylation. *Trends in cell biology*, **13**, 32-42.

Blaskovic, S., Blanc, M. and Goot, F.G. (2013) What does S-palmitoylation do to membrane proteins? *FEBS Journal*, **280**, 2766-2774.

Bleuyard, J.Y., Gallego, M.E. and White, C.I. (2004) Meiotic defects in the Arabidopsis rad50 mutant point to conservation of the MRX complex function in early stages of meiotic recombination. *Chromosoma*. **113**:197-203.

Boursiac, Y., Chen, S., Luu, D.-T., Sorieul, M., van den Dries, N. and Maurel, C. (2005) Early Effects of Salinity on Water Transport in Arabidopsis Roots. Molecular and Cellular Features of Aquaporin Expression. *Plant Physiology*, **139**, 790-805.

Bundock, P. and Hooykaas, P. (2002) Severe developmental defects, hypersensitivity to DNA-damaging agents, and lengthened telomeres in Arabidopsis MRE11 mutants. *The Plant Cell*, **14**, 2451-2462.

Casey, P.J. (1995) Protein lipidation in cell signaling. *Science*, **268**, 221-225.

Caryl, A.P., S.J. Armstrong, G.H. Jones, and F.C. Franklin (2000) A homologue of the yeast HOP1 gene is inactivated in the Arabidopsis meiotic mutant asy1. *Chromosoma*, **109**, 62-71.

Chelysheva, L., Vezon, D., Chambon, A., Gendrot, G., Pereira, L., Lemhemdi, A., Vrielynck, N., Le Guin, S., Novatchkova, M. and Grelon, M. (2012) The Arabidopsis HEI10 is a new ZMM protein related to Zip3. *PLoS Genet*, **8**, e1002799.

Chen, Y. H., Li, H. J., Shi, D.-Q., Yuan, L., Liu, J., Sreenivasan, R., Baskar, R., Grossniklaus, U. and Yang, W.C. (2007) The central cell plays a critical role in pollen tube guidance in Arabidopsis. *The Plant Cell*, **19**, 3563-3577.

Curtis, M.D., Grossniklaus, U. (2003) A Gateway cloning vector set for high-throughput functional analysis of genes in planta. *Plant Physiology*, **133,** 462–469.

De Azevedo Souza, C., Kim, S.S., Koch, S., Kienow, L., Schneider, K., McKim, S.M., Haughn, G.W., Kombrink, E. and Douglas, C.J. (2009) A novel fatty acyl-CoA synthetase is required for pollen development and sporopollenin biosynthesis in Arabidopsis. *The Plant Cell*, **21**, 507-525.

De Muyt, A., Vezon, D., Gendrot, G., Gallois, J.L., Stevens, R. and Grelon, M. (2007) AtPRD1 is required for meiotic double strand break formation in *Arabidopsis thaliana*. *The EMBO journal*, **26**, 4126-4137.

Dobritsa, A.A., Lei, Z., Nishikawa, S.-i., Urbanczyk-Wochniak, E., Huhman, D.V., Preuss, D. and Sumner, L.W. (2010) LAP5 and LAP6 encode anther-specific proteins with similarity to

chalcone synthase essential for pollen exine development in Arabidopsis thaliana. *Plant physiology*, pp. 110.157446.

Earley, K.W., Haag, J.R., Pontes, O., Opper, K., Juehne, T., Song, K. and Pikaard, C.S. (2006) Gateway-compatible vectors for plant functional genomics and proteomics. *The Plant Journal*, **45**, 616-629.

Gabriele A. Fontana, G.A., Hess, D., Reinert, J.K., Mattarocci, S., Benoît Falquet, B., Klein, D., Shore, D., Thomä, N.H., and Rass U. (2019) Rif1 S-acylation mediates DNA double-strand break repair at the inner nuclear membrane. *Nature Communications*, **10**:2535, https://doi.org/10.1038/s41467-019-10349-z

Forrester, M.T., Hess, D.T., Thompson, J.W., Hultman, R., Moseley, M.A., Stamler, J.S. and Casey, P.J. (2011) Site-specific analysis of protein S-acylation by resin-assisted capture. *Journal of lipid research*, **52**, 393-398.

Geldner, N., Dénervaud-Tendon, V., Hyman, D.L., Mayer, U., Stierhof, Y.-D. and Chory, J. (2009) Rapid, combinatorial analysis of membrane compartments in intact plants with a multicolor marker set. *The Plant Journal*, **59**, 169-178.

Greaves, J. and Chamberlain, L.H. (2011) DHHC palmitoyl transferases: substrate interactions and (patho) physiology. *Trends in biochemical sciences*, **36**, 245-253.

Grelon, M., D. Vezon, G. Gendrot, and G. Pelletier. (2001) AtSPO11-1 is necessary for efficient meiotic recombination in plants. *Embo Journal*, **20**, 589-600.

Hemsley, P.A. (2009) Protein S-acylation in plants (Review). *Mol. Membr. Biol.*, **26**, 114-125.

Hemsley, P.A. and Grierson, C.S. (2011) The ankyrin repeats and DHHC S-acyl transferase domain of AKR1 act independently to regulate switching from vegetative to mating states in yeast. *PloS one*, **6**, e28799.

Hemsley, P.A., Kemp, A.C. and Grierson, C.S. (2005) The TIP GROWTH DEFECTIVE1 S-acyl transferase regulates plant cell growth in Arabidopsis. *Plant Cell*, **17**, 2554-2563.

Jefferson, R.A. (1987) Assaying chimeric genes in plants: the GUS gene fusion system. *Plant molecular biology reporter*, **5**, 387-405.

Kho, Y.O. and Baer, J. (1968) Observing pollen tubes by means of fluorescence. *Euphytica*, **17**, 298-302.

Lai, J., Yu, B., Cao, Z., Chen, Y., Wu, Q., Huang, J. and Yang, C. (2015) Two homologous protein S-acyltransferases, PAT13 and PAT14, cooperatively regulate leaf senescence in Arabidopsis. *Journal of Experimental Botany*, **66**, 6345-6353.

Li, Y., Scott, R.J., Doughty, J., Grant, M. and Qi, B. (2015) Protein S-acyltransferase 14: a specific role for palmitoylation in leaf senescence in Arabidopsis. *Plant Physiology*.

Ma, H. (2005) Molecular genetic analyses of microsporogenesis and microgametogenesis in flowering plants. *Annual Reviews of Plant Biology*, **56**, 393-434.

McCormick, S. (2004) Control of male gametophyte development. *The Plant Cell*, **16**, S142-S153.

Mercier, R., Mézard, C., Jenczewski, E., Macaisne, N. and Grelon, M. (2015) The molecular biology of meiosis in plants. *Annual review of plant biology*, **66**, 297-327.

Mitchell, D.A., Vasudevan, A., Linder, M.E. and Deschenes, R.J. (2006) Thematic review series: lipid posttranslational modifications. Protein palmitoylation by a family of DHHC protein S-acyltransferases. *Journal of lipid research*, **47**, 1118-1127.

Puizina, J., Siroky, J., Mokros, P., Schweizer, D., Riha K. (2004) Mre11 deficiency in Arabidopsis is associated with chromosomal instability in somatic cells and Spo11-dependent genome fragmentation during meiosis. *Plant Cell*, **16**, 1968-1978.

Qi, B., Doughty, J. and Hooley, R. (2013) A Golgi and tonoplast localized S-acyl transferase is involved in cell expansion, cell division, vascular patterning and fertility in Arabidopsis. *New Phytologist*, **200**, 444-456.

Ren, J., Wen, L., Gao, X., Jin, C., Xue, Y. and Yao, X. (2008) CSS-Palm 2.0: an updated software for palmitoylation sites prediction. *Protein Engineering Design and Selection*, **21**, 639-644.

Resh, M.D. (2006) Palmitoylation of ligands, receptors, and intracellular signaling molecules. *Science Signaling*, **2006**, re14-re14.

Rodriguez-Enriquez, M., Mehdi, S., Dickinson, H. and Grant-Downton, R. (2013) A novel method for efficient in vitro germination and tube growth of Arabidopsis thaliana pollen. *New Phytologist*, **197**, 668-679.

Sanders, P.M., Bui, A.Q., Weterings, K., McIntire, K., Hsu, Y.-C., Lee, P.Y., Truong, M.T., Beals, T. and Goldberg, R. (1999) Anther developmental defects in Arabidopsis thaliana male-sterile

Silvius, J.R. and l'Heureux, F. (1994) Fluorometric evaluation of the affinities of isoprenylated peptides for lipid bilayers. *Biochemistry*, **33**, 3014-3022.

Valdez-Taubas, J. and Pelham, H. (2005) Swf1-dependent palmitoylation of the SNARE Tlg1 prevents its ubiquitination and degradation. *The EMBO journal*, **24**, 2524-2532.

Wan, Z., Sen S., Ge, F., Feng, F., Yan, Z., Sha, L. (2017) Arabidopsis PROTEIN S-ACYL TRANSFERASE4 mediates root hair growth. The Plant Journal, 90, 249-260

Yuan, X., Zhang, S., Sun, M., Liu, S., Qi, B. and Li, X. (2013) Putative DHHC-Cysteine-Rich Domain S-Acyltransferase in Plants. *PloS one*, **8**.

Zhao, X.Y., Wang, J.G., Song, S.J., Wang, Q., Kang, H., Zhang, Y. and Li, S. (2016) Precocious leaf senescence by functional loss of PROTEIN S-ACYL TRANSFERASE14 involves the NPR1-dependent salicylic acid signaling. *Scientific reports*, **6**.

Zhou, F., Xue, Y., Yao, X. and Xu, Y. (2006) CSS-Palm: palmitoylation site prediction with a clustering and scoring strategy (CSS). *Bioinformatics*, **22**, 894-896.

Zhou, L.Z., Li, S., Feng, Q.N., Zhang, Y.L., Zhao, X., Zeng, Y.l., Wang, H., Jiang, L. and Zhang, Y. (2013) PROTEIN S-ACYL TRANSFERASE10 Is Critical for Development and Salt Tolerance in Arabidopsis. *The Plant Cell*, **25**, 1093-1107.

FIGURE LEGENDS

Figure 1. AtPAT21 is an S-acyltransferase by yeast complementation and Acyl-RAC assay.

(a) DIC light (upper panel) and UV microscopy of DAPI (1µg/ml) stained cells (lower panel) of all 4 genotypes grown at 37ºC. Arrows indicate multiple nuclei. Cells were transformed with empty vector pYES2 (WT and *akr1*), or with AtPAT21 and AtPAT21C^{174}S (*akr1*-PAT21, *akr1*-PAT21C^{174}S). Scale bars: 10 µm.

(b) AtPAT21 is auto-acylated. AtPAT21 and AtPAT21C^{174}S were detected by Western blotting with an anti-V5 antibody using the ECL method. The molecular weight of AtPAT21 and AtPAT21C^{174}S is ~70 kDa. A band corresponding to AtPAT21-V5 was detected in the + NH_2OH treated sample, indicating that it is bound to an acyl group via a labile thioester linkage confirming that it is auto-acylated. However, no signal was detected for AtPAT21C^{174}S indicating that it is not auto-acylated. LC: loading control, Lane +: NH_2OH treated and Lane -: non NH_2OH treated.

Figure 2. AtPAT21 is localised to the plasma membrane. Confocal microscopy observation of the primary root of 7-day-old seedlings derived from 35S:AtPAT21-YFP complemented atpat21-1 plants that were crossed with the plasma membrane marker Waveline R138. Scale bar: 10 µm

Figure 3. Isolation and characterization of AtPAT21 T-DNA insertion mutant.

(a) Schematic presentation of the AtPAT21 gene (solid boxes represent exons, empty boxes untranslated regions and lines introns) and the positions of the T-DNA in *atpat21-1* mutant line SALK_016521. The positions of the primers used for RT-PCR (Beg and End) and genotyping (LP1 and RP1) are indicated. RB, right border; LB, left border.

(b) Amplification of the full length of AtPAT21 transcript in wild-type and *atpat21-1* plants using primers Beg and End shown in A. The *GAPc* transcript served as a control.

(c) & (d) 4- and 6-week-old WT Col-0 (left) and *atpat21-1* (right).

(e) Leaf line-ups of 25-day old WT Col-0 (Top) and *atpat21-1* (bottom) plants.

(f) AtPAT21 can complement the phenotype of *atpat21-1* but AtPAT21C^{174}S can not. Seven out of 24 and 5 out of 20 transformants were recovered from the AtPAT21 and AtPAT21C^{174}S expressing lines, respectively where all of which were homozygous for the T-DNA as well as harbour the respective transgenes. A representative plant from each genotype of 4-week old plants was photographed and shown.

Figure 4. Defects in the reproduction tissues of *atpat21-1*.

(a-c) WT. (d-f) *atpat21-1*.

(a)&(d) Fully opened flowers.

(b)&(e) anthers observed by scanning electronic microscopy (SEM).

(c)&(f) pollen grains observed by SEM (main pictures, bars, 5µm) and DAPI-stained pollen grains under UV (insets at right bottom corner, bars, 20µm). Arrows in (a) & (d) indicate the position of the anthers from WT and *pat21-1* flowers.

Figure 5. Different developmental stages of WT and *atpat21-1* mutant anthers to show that he *atpat21-1* mutant pollen grains start to degenerate after release from tetrad.

(a-d) WT. (e-h) *atpat21-1*.
(a)&(e) Meiosis stage.
(b)&(f) Tetrad stage.
(c)&(g) pollen grains released from tetrad.
(d)&(h) pollen grains.
E, epidermis; EN, endothecium; ML, middle layer; T, tapetum; M, Meiocyte; Tds, tetrad; PG, pollen grain; dPG, degenerated pollen grain. Scale bars: 10μm.

Figure 6. *atpat21-1* has female gametophytic defects. WT and *atpat21-1* stigmas were hand-pollinated with plenty of WT pollen and the embryo development and pollen tube growth were observed.

(a) Ovules were cleared and the embryo development was observed at 0, 1 and 2 days after pollination (DAP). The mature siliques at 15 DAP were also opened and the seed set was observed. Arrows indicate embryos in WTxWT ovules. At least 3 siliques at each time point of development were opened and observed. Scale bars: 20μm.
(b) Aniline blue stained WT pollen tubes on stigmas and styles of WT and *atpat21-1*. Top: ♀WT x WT♂. Arrow shows WT pollen tube entering the WT ovule through the micopyle (arrowhead). Bottom: ♀*pat21* x WT♂. WT pollen tube (Arrows) failed to find and enter the micropyle (arrowhead) of *atpat21-1* ovule.

Figure 7. Male and female gametophytic defects observed in heterozygous *atpat21-1* (+/-).

(a) Defects in male gametes of *atpat21-1*. Pollen (left) and *in vitro* pollen tube growth assay (right). Red arrows indicate smaller pollen grains that are probably derived from the mutant allele. Approximately 87.3% of the WT pollen grains were germinated yet only about 47.8% of heterozygous pollen grains germinated. The pollen germination assays were carried out three times. The representative images shown here are from one of these assays. Scale bars: 0.1mm.
(b) Defects in female gametes. Observation of female gametophytes the *atpat21-1* (+/-) using confocal laser scanning microscope (CLSM). 1, normal gametophyte of the WT allele at FG7 with a functional 8-celled embryo sac (cc, central cell, ec, egg cell, sc, synergid cells); 2-3, abnormal gametophytes that are probably derived from the mutant allele at FG7. Arrows in 3 indicate cells without clear specification; 4-5, normal megaspore specification of the WT allele from FG1 to FG2. Arrows in 4&5 indicate megaspore and divided megaspore; 6-9, gametophytes with different defects that are probably derived from the mutant allele at FG1 to FG2 stage. Arrow in 6, 8&9 indicate abnormal megaspore, arrow in 7 indicates a central vacuole formed in place of the megaspore. Scale bars: 20μm

Figure 8. Meiotic atlases of DAPI stained chromosomal spreads from WT (a-e), *pat21-1* (f-i), *spo11-1* (k-o) and *pat21-1/spo11-1* (p-t) plants.

Representative cells from five different meiotic substages are shown for each genotype. Mitotic anaphase cells are shown from WT (u) and *pat-21* cells (v). 17% of *pat21-1* anaphase cells contain lagging chromosomes or anaphase bridges as shown in (v). The number of cells observed at each stage in each genotype (n) is labelled in every image. Cells were obtained from buds pooled from at least 3 plants of each genotype. Scale bars = 5 μm.

Table 1. Ratios of different genotypes observed in the F1 progeny of different crosses.

Crosses	Genotype	Expected ratio	Observed
♀Het x ♂Het (Selfed)	AtPAT21(+/+) and *atpat21*(+/-):*atpat21*(-/-)	3:1	5.2:1 (178:34)
♀WT x ♂Het	AtPAT21(+/+):*atpat21*(+/-)	1:1	1.3:1 (84:65)
♀ Het x ♂WT	AtPAT21(+/+):*atpat21*(+/-)	1:1	1.9:1 (95:50)

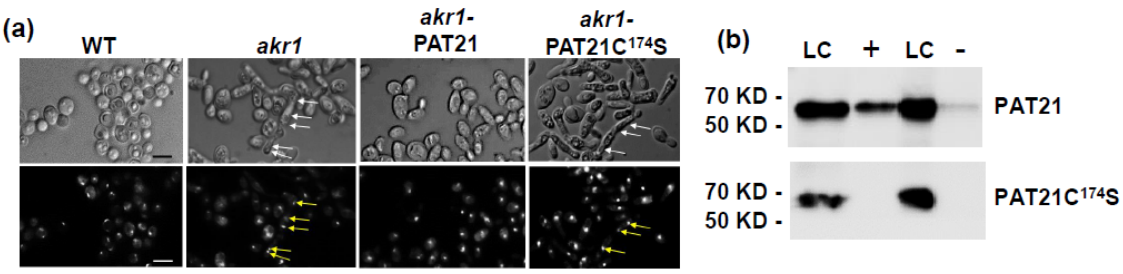

Figure 1. AtPAT21 is an S-acyltransferase by yeast complementation and Acyl-RAC assay.

(a) DIC light (upper panel) and UV microscopy of DAPI (1µg/ml) stained cells (lower panel) of all 4 genotypes grown at 37°C. Arrows indicate multiple nuclei. Cells were transformed with empty vector pYES2 (WT and *akr1*), or with AtPAT21 and AtPAT21C^{174}S (*akr1*-PAT21, *akr1*-PAT21C^{174}S). Scale bars: 10 µm.

(b) AtPAT21 is auto-acylated. AtPAT21 and AtPAT21C^{174}S were detected by Western blotting with an anti-V5 antibody using the ECL method. The molecular weight of AtPAT21 and AtPAT21C^{174}S is ~70 kDa. A band corresponding to AtPAT21-V5 was detected in the + NH_2OH treated sample, indicating that it is bound to an acyl group via a labile thioester linkage confirming that it is auto-acylated. However, no signal was detected for AtPAT21C^{174}S indicating that it is not auto-acylated. LC: loading control, Lane +: NH_2OH treated and Lane -: non NH_2OH treated.

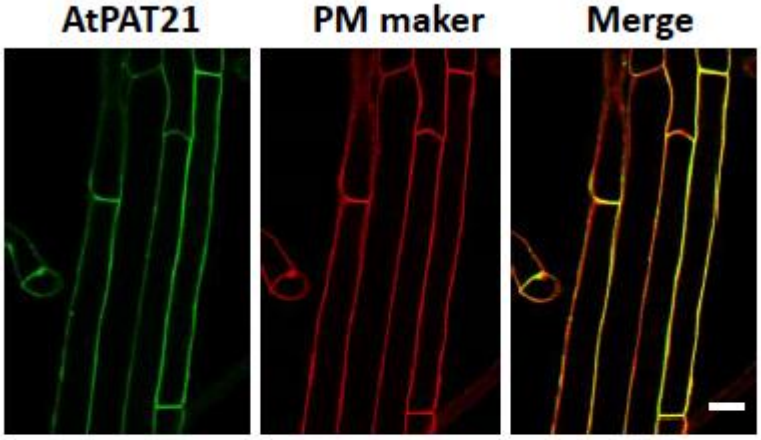

Figure 2. AtPAT21 is localised to the plasma membrane. Confocal microscopy observation of the primary root of 7-day-old seedlings derived from 35S:AtPAT21-GFP complemented *atpat21-1* plants that were crossed with the plasma membrane marker Waveline R138. Scale bar: 10 µm

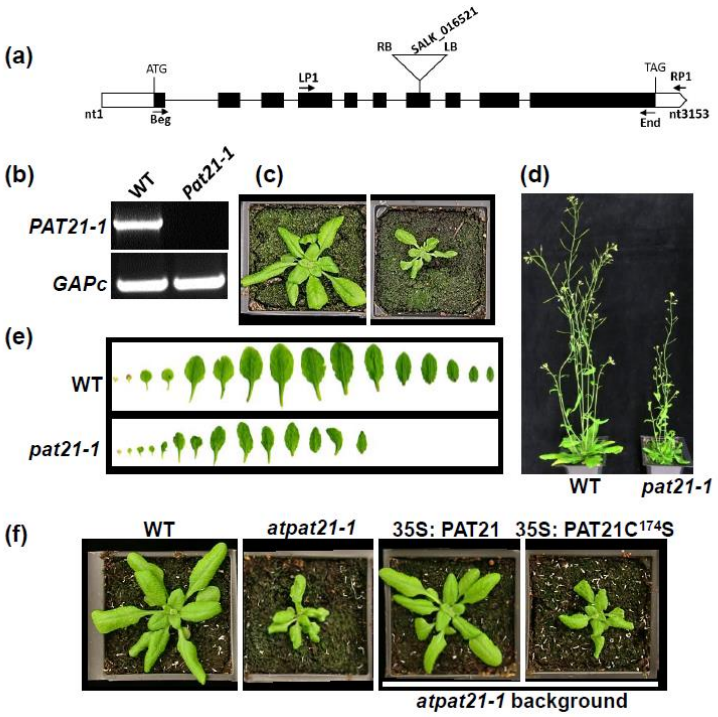

Figure 3. Isolation and characterization of AtPAT21 T-DNA insertion mutant.

(a) Schematic presentation of the AtPAT21 gene (solid boxes represent exons, empty boxes untranslated regions and lines introns) and the positions of the T-DNA in *atpat21-1* mutant line SALK_016521. Arrows indicate the primers (Beg and End) used for RT-PCR and primers (LP1 and RP1) for genotyping PCR. RB, right border; LB, left border.

(b) Amplification of the full length of AtPAT21 transcript in wild-type and *atpat21-1* plants using primers Beg and End shown in A. The *GAPc* transcript served as a control.

(c) & (d) 4- and 6-week-old WT Col-0 (left) and *atpat21-1* (right).

(e) Leaf line-ups of 25-day old WT Col-0 (Top) and *atpat21-1* (bottom) plants.

(f) AtPAT21 can Complement the phenotype of *atpat21-1* but AtPAT21C^{174}S can not. Seven out of 24 and 5 out of 20 transformants were recovered from the AtPAT21 and AtPAT21C^{174}S expressing lines, respectively where all of which were homozygous for the T-DNA as well as harbour the respective transgenes. A representative plant from each genotype of 4-week old plants was photographed and shown.

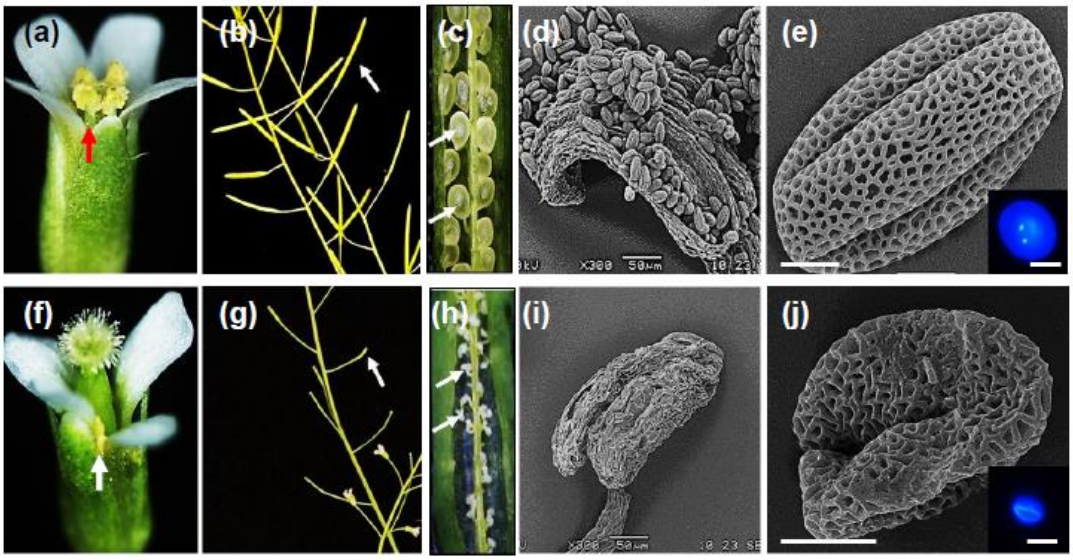

Figure 4. Defects in the reproduction tissues of *atpat21-1*.
(a-e) WT. (f-j) *atpat21-1*.
(a)&(f) Fully opened flowers.
(b)&(g) fully elongated siliques (arrows).
(c)&(h) 2 days after naturally pollinated ovules (arrows).
(d)&(i) anthers observed by scanning electronic microscopy (SEM).
(e)&(j) pollen grains observed by SEM (main pictures, bars, 5μm) and DAPI-stained pollen grains under UV (insets at right bottom corner, bars, 20μm). Arrows in (a) & (f) indicate the position of the anthers from WT and *pat21-1* flowers.

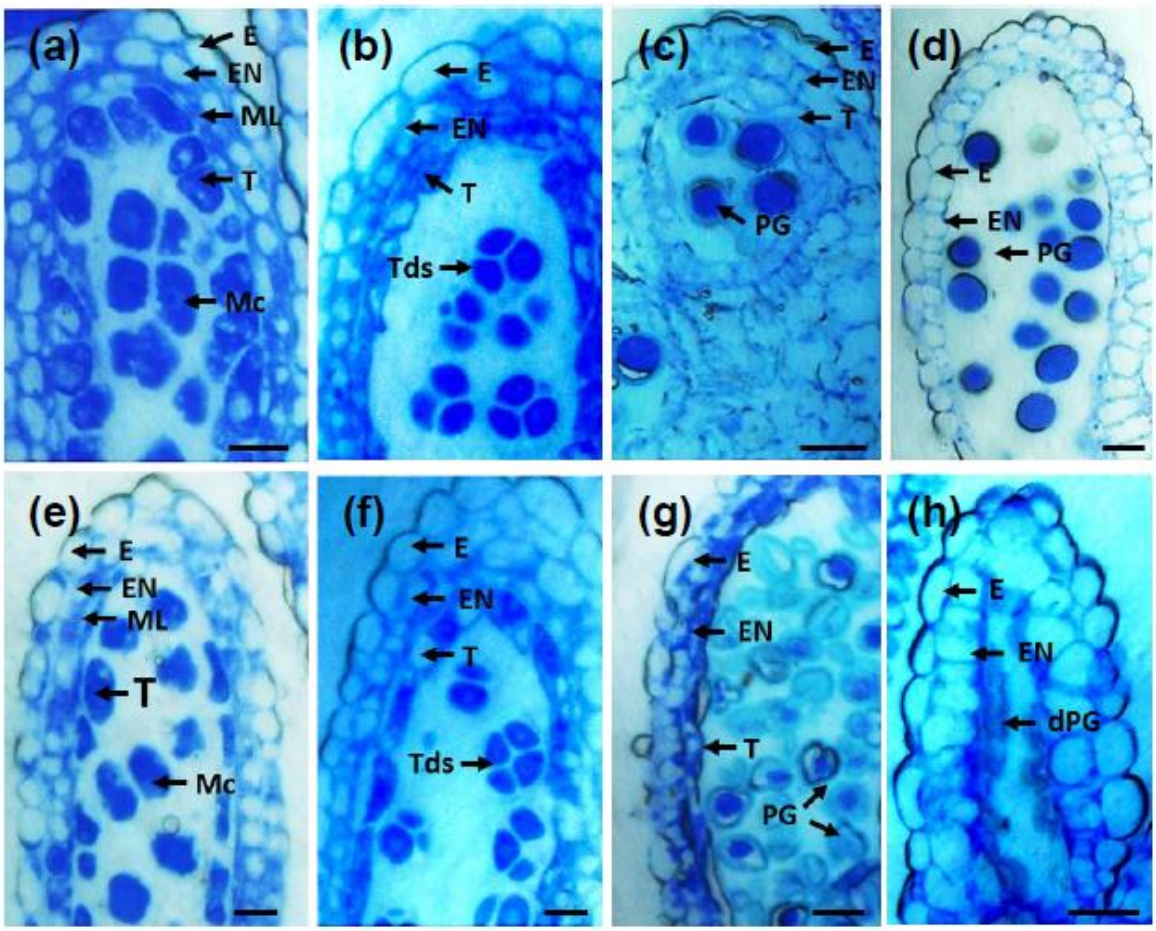

Figure 5. Different developmental stages of WT and *atpat21-1* mutant anthers to show that he *atpat21-1* mutant pollen grains start to degenerate after release from tetrad.
(a-d) WT. (e-h) *atpat21-1*.
(a)&(e) Meiosis stage.
(b)&(f) Tetrad stage.
(c)&(g) pollen grains released from tetrad.
(d)&(h) pollen grains.
E, epidermis; EN, endothecium; ML, middle layer; T, tapetum; M, Meiocyte; Tds, tetrad; PG, pollen grain; dPG, degenerated pollen grain. Scale bars: 10μm.

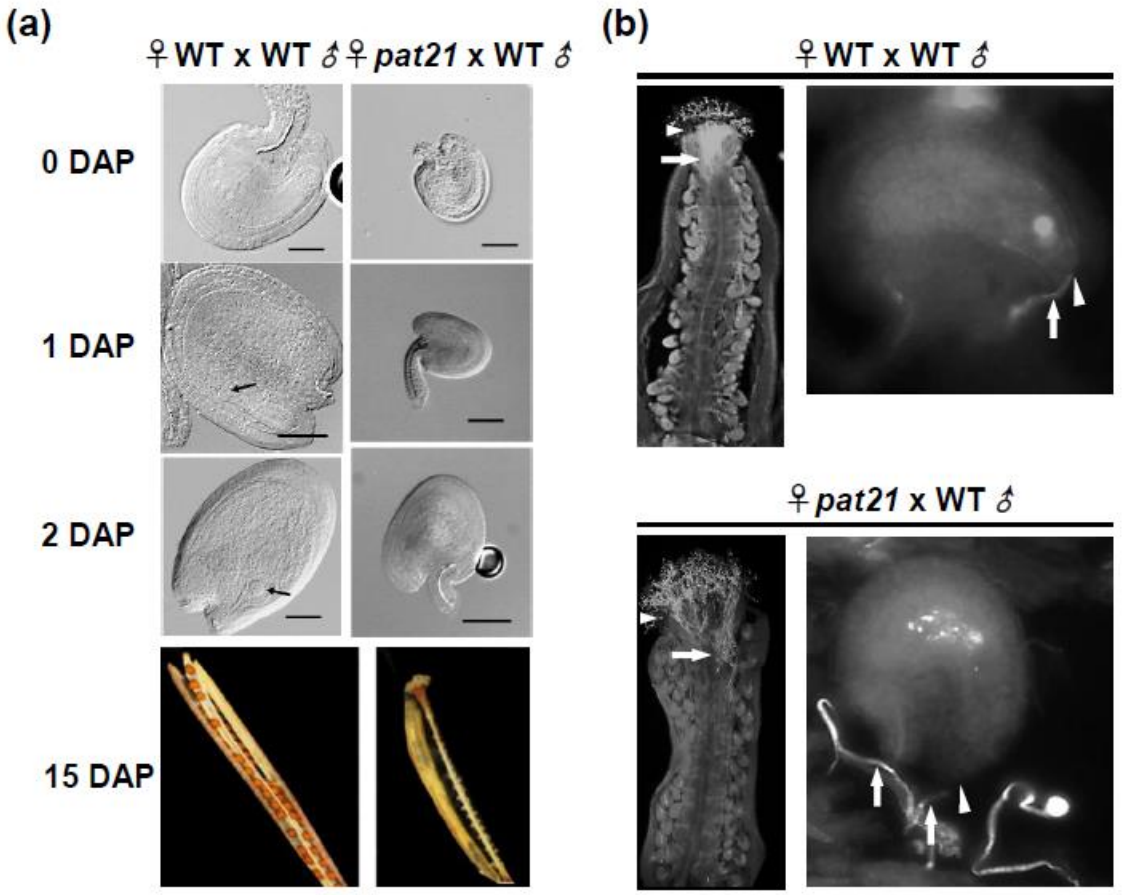

Figure 6. *atpat21-1* has female gametophytic defects. WT and *atpat21-1* stigmas were hand-pollinated with plenty of WT pollen and the embryo development and pollen tube growth were observed.

(a) Ovules were cleared and the embryo development was observed at 0, 1 and 2 days after pollination (DAP). The mature siliques at 15 DAP were also opened and the seed set was observed. Arrows indicate embryos in WTxWT ovules. Scale bars: 20μm.

(b) Aniline blue stained WT pollen tubes on stigmas and styles of WT and *atpat21-1*. Top: ♀WT x WT♂. Arrow shows WT pollen tube entering the WT ovule through the micopyle (arrowhead). Bottom: ♀*pat21* x WT♂. WT pollen tube (Arrows) failed to find and enter the micropyle (arrowhead) of *atpat21-1* ovule.

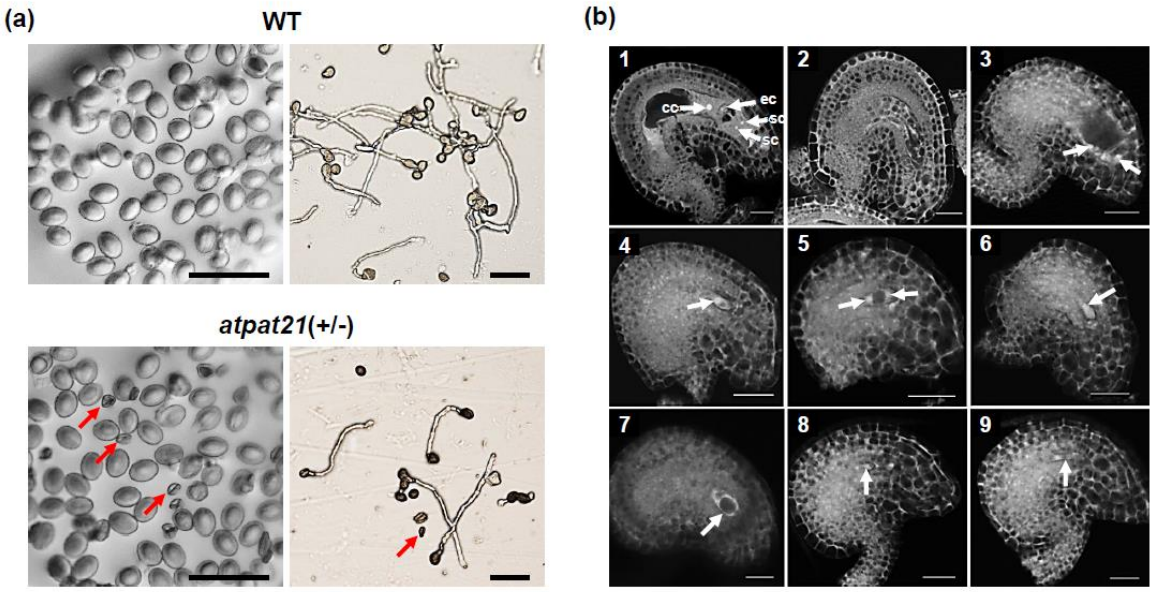

Figure 7. Male and female gametophytic defects observed in heterozygous *atpat21-1* (+/-).

(a) Defects in male gametes of *atpat21-1*. Pollen (left) and *in vitro* pollen tube growth assay (right). Red arrows indicate smaller pollen grains that are probably derived from the mutant allele. Approximately 87.3% of the WT pollen grains were germinated yet only about 47.8% of heterozygous pollen grains germinated. Scale bars: 0.1mm.

(b) Defects in female gametes. Observation of female gametophytes the *atpat21-1* (+/-) using confocal laser scanning microscope (CLSM). 1, normal gametophyte of the WT allele at FG7 with a functional 8-celled embryo sac (cc, central cell, ec, egg cell, sc, synergid cells); 2-3, abnormal gametophytes that are probably derived from the mutant allele at FG7. Arrows in 3 indicate cells without clear specification; 4-5, normal megaspore specification of the WT allele from FG1 to FG2. Arrows in 4&5 indicate megaspore and divided megaspore; 6-9, gametophytes with different defects that are probably derived from the mutant allele at FG1 to FG2 stage. Arrow in 6, 8&9 indicate abnormal megaspore, arrow in 7 indicates a central vacuole formed in place of the megaspore. Scale bars: 20μm

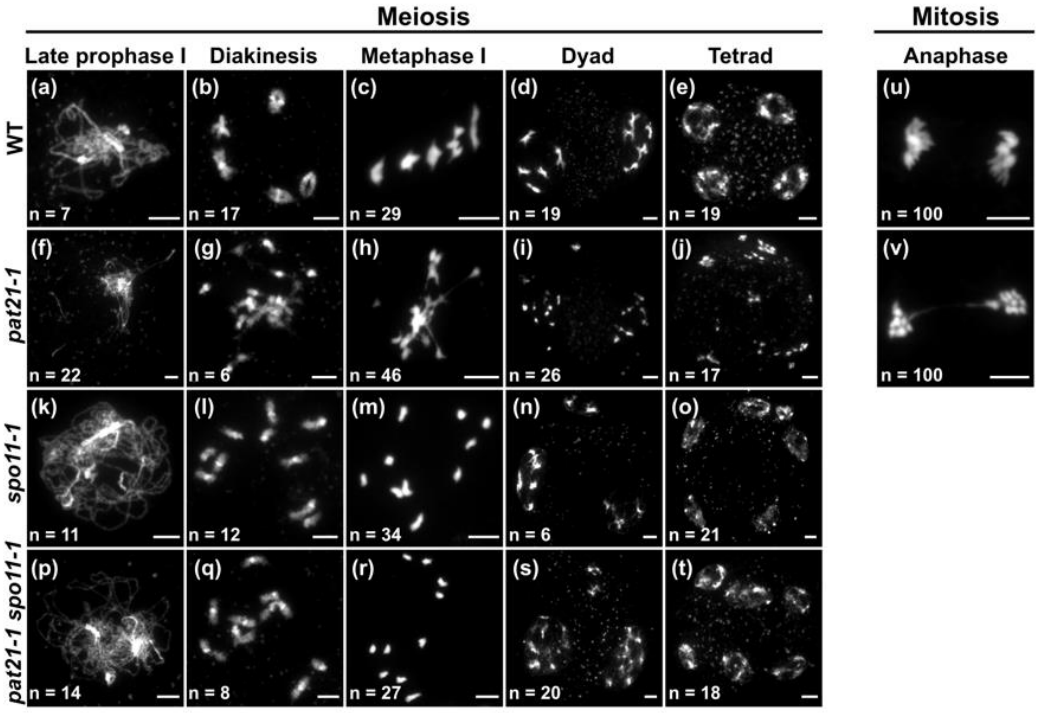

Figure 8. Meiotic atlases of DAPI stained chromosomal spreads from WT (A-E), *pat21-1* (F-I), *spo11-1* (K-O) and *pat21-1/spo11-1* (P-T) plants. Representative cells from five different meiotic substages are shown for each genotype. Mitotic anaphase cells are shown from WT (U) and *pat-21* cells (V). 17% of *pat21-1* anaphase cells contain lagging chromosomes or anaphase bridges as shown in (V). The number of cells observed at each stage in each genotype (n) is labelled in every image. Cells were obtained from buds pooled from at least 3 plants of each genotype. Scale bars = 5 µm.

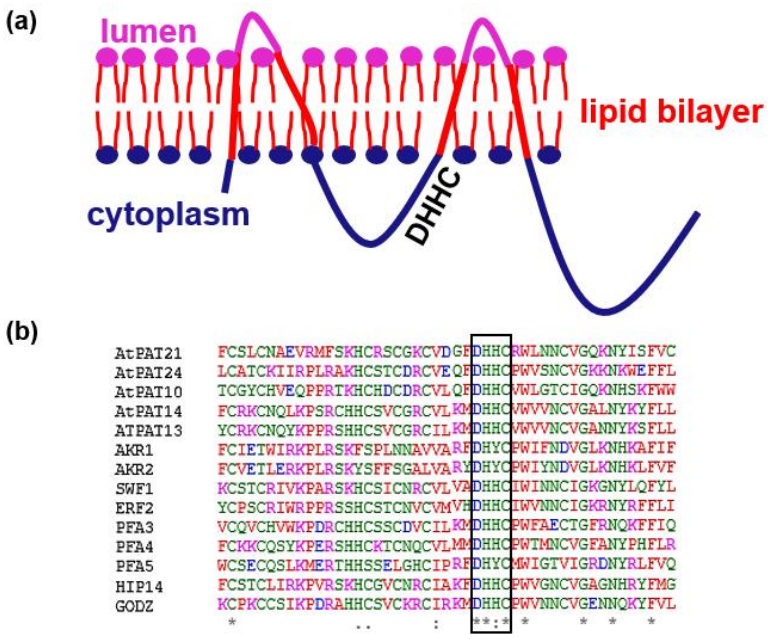

Figure S1. Secondary structure prediction of AtPAT21 and protein sequence alignment of some known DHHC-PATs.

(a) Secondary structure prediction of AtPAT21 shows that it has 4 transmembrane domains, and DHHC-CRD as well as both the C- and N-termini are localised in the cytosol.

(b) AtPAT21 shares sequence homology at the DHHC-CRD region with other known PATs from Arabidopsis, yeast and mammals. The DHHC motif is boxed. AtPAT21: ACCESSION NP_180922, AtPAT24 (TIP1): ACCESSION NP_197535, AtPAT10: ACCESSION NP_566950.1, AtPAT14: ACCESSION NP_191639, AtPAT13: ACCESSION NP_567668, AKR1: ACCESSION NP_010550, AKR2: ACCESSION NP_014677, SWF1: ACCESSION NP_010411, ERF2: ACCESSION Q06551, PFA3: ACCESSION NP_014073, PFA4: ACCESSION NP_014640, PFA5: ACCESSION NP_010747, HIP14 (DHHC17): ACCESSION AAH50324, GODZ (DHHC3): ACCESSION NP_057682.

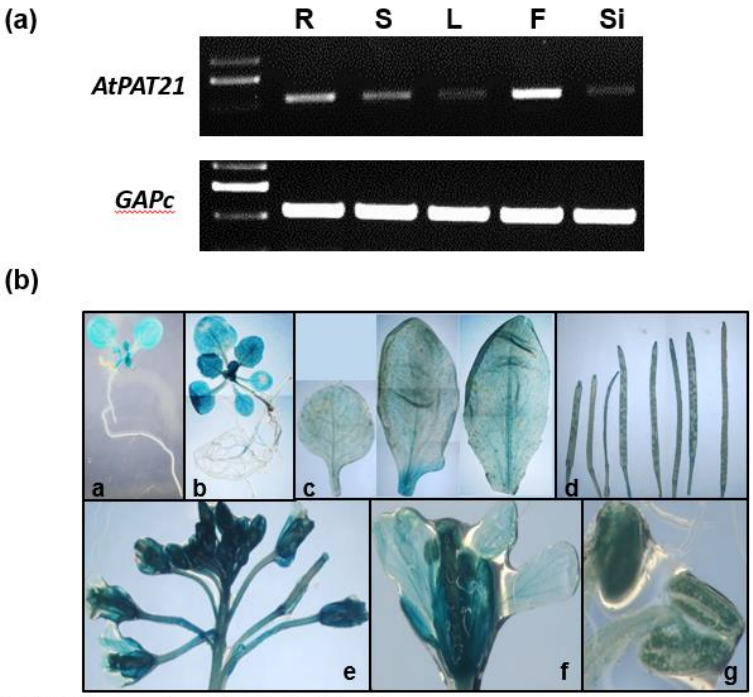

Figure S2. AtPAT21 expression pattern in Arabidopsis.

(a) Transcript levels of AtPAT21 in different tissues. RT-PCR was carried out on total RNA isolated from different parts of WT plant in different developmental stages. R, roots of 2-week old seedlings grown on the 1/2 MS plate; S, stem of the first node of 35-day old soil-grown plants; L, the 5th and 6th rosette leaves of 4-week old soil-grown plants; F, fully-opened flowers; Si, 3-day-old siliques after pollination.

(b) Histochemical localization of AtPAT21. GUS-staining analysis was carried out in different part of the transgenic Arabidopsis plant harbouring the AtPAT21promoter:GUS fusion construct. a, 1-week old seedlings; b, 2-week old seedlings; c, rosette leaves from 5-week old plant, young (left) to old (right); d, different stages of siliques, from 2 days (left) to 8 days (right) after pollination; e&f, Inflorescence and flower from 5-week old plants; g, anthers.

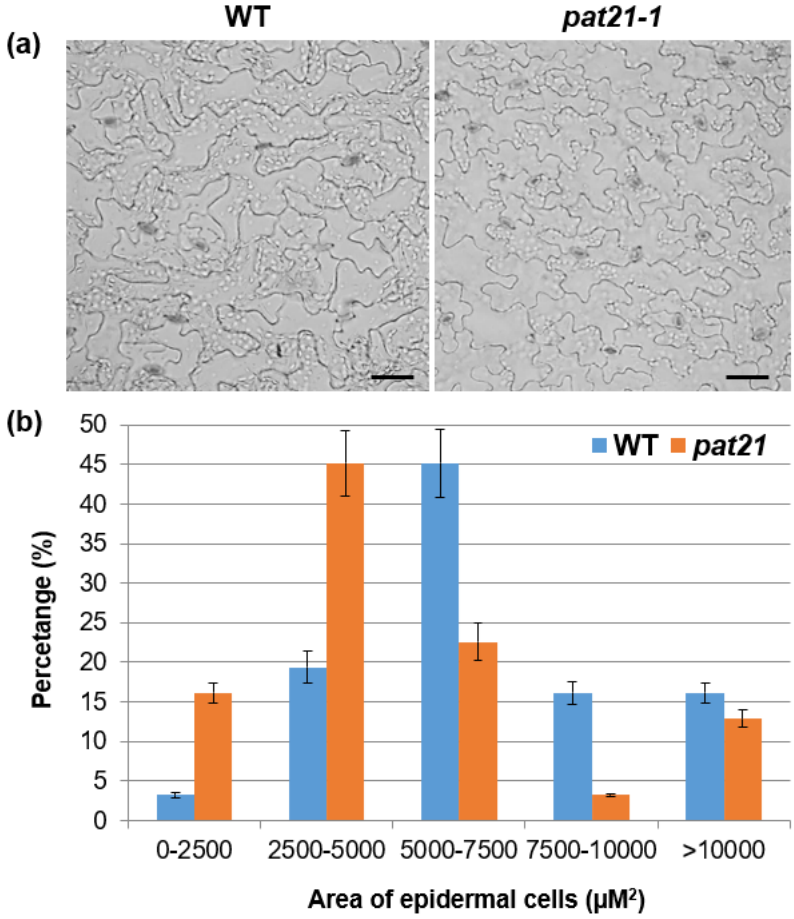

Figure S3. *atpat21-1* has smaller cells.

(a) Epidermal cells. Bars, 50μm.

(b) Percentage of cells within different size ranges. Cells from epidermal peels of 3 mature leaves were measured and assigned to different groups according to their sizes as indicated in the figure (n=100 from each leaf). Error bars show standard error on the means.

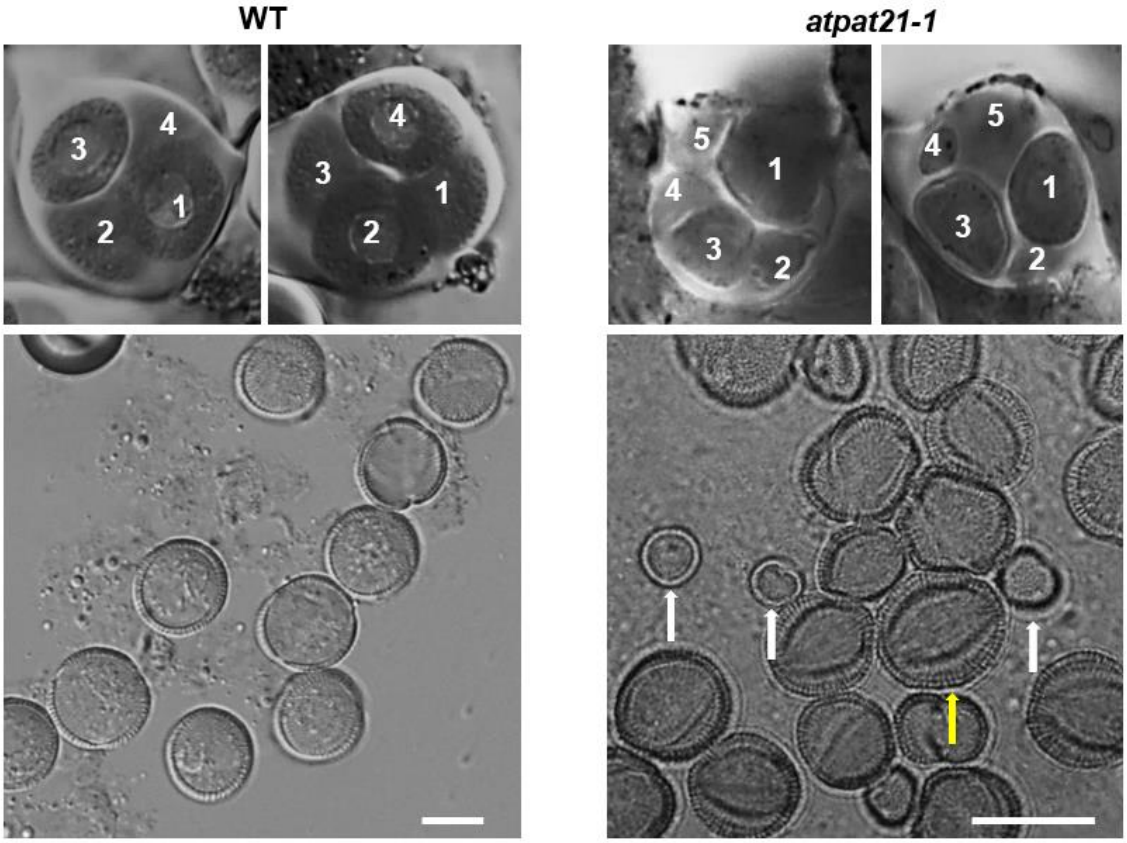

Figure S4. The *atpat21-1* mutant have asymmetrical polyads structure which will release variable sizes of pollen grains.
Top, tetrads; bottom, pollen grains. Numbers indicate individual microspores; White arrows indicate smaller pollen grains and yellow indicates normal and larger size pollen grain. Bars: 25μm.

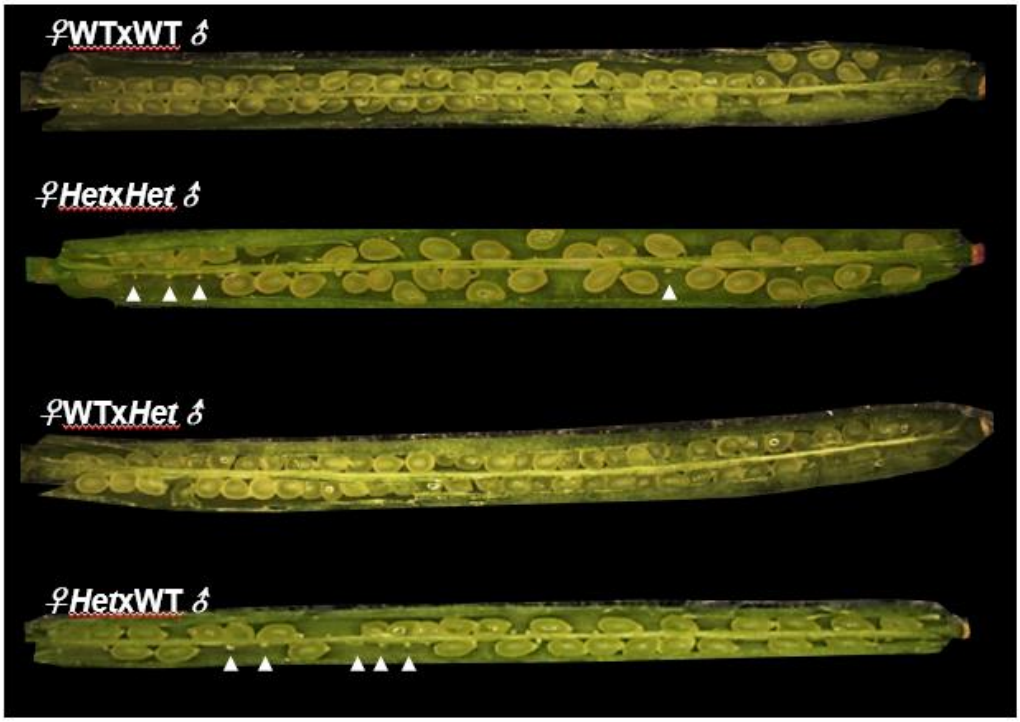

Figure S5. Seed set of different crosses. 7-day-old siliques after hand pollination were opened. White arrowheads indicate un-fertilized ovules.

Table S1. Phenotypic analysis of WT and *atpat21* Arabidopsis.

	WT	***atpat21***
Plant height (mm)	476.0±18.9	441.9±7.4
No. of inflorescences per plant	23.0±2.8	67.1±6.2
No. of siliques in main branch	55.8±1.9	63.3±3.3
Length of silique (mm)	17.0±0.7	3.0±0

Data were collected from 8-week old plants of WT and the mutant (n=20). The length of the 10th silique counted from the base of the main branch was measured (n=40). Values are average±SD.

Supplemental Table S2. Sequence of primers used in this study.

primer	Sequence
LBb1	5’-GCGTGGACCGCTTGCTGCAACT-3’
SALK016521LP1	5’-TGGGCCATATATTAGACACGG-3’
SALK016521RP1	5’-GCTTGCAGGTGAAGGATACTG-3’
Beg	5’-CAAAAAAGCAGGCTCCACCATGGCGAGAAGACATGGATG-3’
End	5’-CAAGAAAGCTGGGTCATGGAATCTAGTAGATAAATG-3’
GAPc For	5’-CACTTGAAGGGTGGTGCCAAG-3’
GAPc Rev	5’-CCTGTTGTCGCCAACGAAGTC-3’
DHHCtoS For	5’-GGTTTGATCACCATTCCCGGTGGCTGAATAAC-3’
DHHCtoS Rev	5’-GTTATTCAGCCACCGGAATGGTGATCAAACC-3’
pPAT21attB1	5’-CAAAAAAGCAGGCTCCACCTTTCTTCTTCTCTCTCTCAAAAGTTGACC-3’
pPAT21attB2	5’-CAAGAAAGCTGGGTCCATTGCAATGAAGAAACCCACAA-3’
attB1	5’-GGGGACAAGTTTGTACAAAAAAGCAGGCT-3’
attB2	5’-GGGGACCACTTTGTACAAGAAAGCTGGGT-3’

Supplemental Table S2. Prediction by CSS-PALM of potential *S*-acylated cysteines of encoded proteins of some meiosis related genes.

Protein	AGI No.	Position of S-acylated cysteines	Score*	references
MEI1	AT1G77320	C41, C42, C97	9.13, 7.4, 4.70	Mathilde et al., 2003
SWI1	AT5G51330	Not available		Mercier et al., 2001 and 2003
CDC45	AT3G25100	C524, C526	3.97, 4.94	Stevens et al., 2004
XRI1	AT5G48720	C202	5.18	Dean et al., 2009
SPO11	AT1G63990	C107, C128	5.27, 4.24	Stacey et al., 2006
PRD1	AT1G01690	C9	33.55	De Muyt et al., 2007
DFO	AT1G07060	C118	4.77	Zhang et al., 2012
PHS1	AT1G10710	C378, C379, C402	8.79, 5.59, 12.29	Ronceret et al., 2009
MRE11	AT5G54260	C18	26.07	Bundock and Hooykaos, 2002
RAD50	AT2G31970	C46, C697, C698	11.81, 6.70, 7.45	Bleuyard et al., 2004
RAD51	AT5G20850	Not available		Li et al., 2004
XRCC3	AT5G57450	Not available		Bleuyard and White, 2004
GR1	AT3G52115	C267, C339	3.747, 4.39	Vanschou et al., 2007
MCM8	AT3G09660	C107, C183, C464	10.98, 5.11, 7.51	Crismani et al., 2013
DMC1	AT3G22880	Not available		Couteau et al., 1999
AHP2	AT1G13330	Not available		Schommer et al., 2003
MND1	AT4G29170	Not available		Kerzendorfer et al., 2006
SDS	AT1G14750	C568	11.21	Yoshitaka et al., 2002
BLAP75	AT5G63540	C154	4.27	Chelysheva et al., 2008
RFC1	AT5G22020	C687, C688	7.06, 5.75	Liu et al., 2013
TOP3α	AT5G63920	C602, C645	4.74, 4.01	Hartung et al., 2008
MSH2	AT3G18524	C930	16.47	Emmanuel et al., 2006

RBR	AT3G12280	C440, C504, C788, C789	4.01, 4.30, 12.63, 8.64	Chen et al., 2011
ZIP4	AT5G48390	Not available		Chelysheva et al., 2007
MER3	AT3G27730	Not available		
HEI10	AT1G53490	C3, C6	19.68, 40.15	Chelysheva et al., 2012
MLH1	AT4G09140	C262, C467, C468	11.99, 7.40, 4.24	Dion et al., 2007
ASY1	AT1G67370	Not available		Caryl et al., 1999
SCC3	AT2G47980	C610, C804	13.36, 4.11	Chelysheva et al., 2005
CTF7	AT4G31400	Not available		Jauh et al., 2013
PANS1	AT3G14190	Not available		Juraniec et al., 2015
AESP	AT4G22970	C1182, C1226, C1477, C1478	5.48, 7.27, 6.93, 16.07	Liu and Makaroff, 2006
CYCA1	AT1G77390	C339	3.895	Wang et al., 2004; Jha et al., 2004
OSD1	AT3G57860	C156	14.30	Cromer et al., 2012
SMG7	AT5G19400	C173, C451, C452	11.79, 5.09, 6.76	Rieh et al., 2008

* The similarity to a known palmitoylation site.